Inorganic Chemistry

pubs.acs.org/IC
Article

The Unique Role of the Second Coordination Sphere to Unlock and Control Catalysis in Nonheme Fe(II)/2-Oxoglutarate Histone Demethylase KDM2A

Midhun George Thomas, Simahudeen Bathir Jaber Sathik Rifayee, Shobhit S. Chaturvedi, Koteswara Rao Gorantla, Walter White, Jon Wildey, Christopher J. Schofield, and Christo Z. Christov*

Cite This: *Inorg. Chem.* 2024, 63, 10737−10755

Read Online

ACCESS | Metrics & More | Article Recommendations | Supporting Information

ABSTRACT: Nonheme Fe(II) and 2-oxoglutarate (2OG)-dependent histone lysine demethylases 2A (KDM2A) catalyze the demethylation of the mono- or dimethylated lysine 36 residue in the histone H3 peptide (H3K36me1/me2), which plays a crucial role in epigenetic regulation and can be involved in many cancers. Although the overall catalytic mechanism of KDMs has been studied, how KDM2 catalysis takes place in contrast to other KDMs remains unknown. Understanding such differences is vital for enzyme redesign and can help in enzyme-selective drug design. Herein, we employed molecular dynamics (MD) and combined quantum mechanics/molecular mechanics (QM/MM) to explore the complete catalytic mechanism of KDM2A, including dioxygen diffusion and binding, dioxygen activation, and substrate oxidation. Our study demonstrates that the catalysis of KDM2A is controlled by the conformational change of the second coordination sphere (SCS), specifically by a change in the orientation of Y222, which unlocks the 2OG rearrangement from off-line to in-line mode. The study demonstrates that the variant Y222A makes the 2OG rearrangement more favorable. Furthermore, the study reveals that it is the size of H3K36me3 that prevents the 2OG rearrangement, thus rendering the enzyme inactivity with trimethylated lysine. Calculations show that the SCS and long-range interacting residues that stabilize the HAT transition state in KDM2A differ from those in KDM4A, KDM7B, and KDM6A, thus providing the basics for the enzyme-selective redesign and modulation of KDM2A without influencing other KDMs.

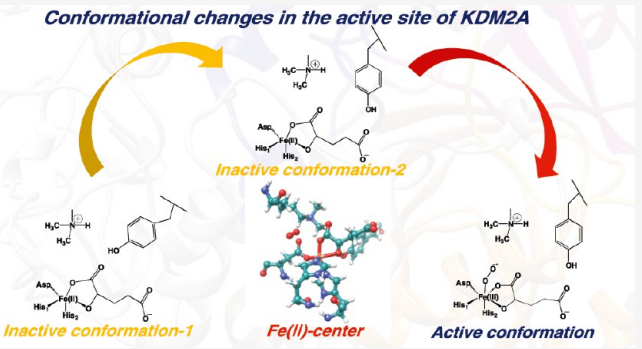

1. INTRODUCTION

N^{ϵ}-Methylation of lysine residues in histone tails is important in the regulation of eukaryotic transcription,[1] and its misregulation is related to diseases, including cancer and genetic disorders.[2−6] The histone methylation status is maintained by the activities of two groups of enzymes, histone lysine methyltransferases and histone demethylases.[7−9] Histone lysine demethylases (KDMs) are grouped into families from KDM1−9.[10−13] KDM1s belong to flavin adenine dinucleotide (FAD)-dependent enzymes,[14] and KDM2−9 are Jumonji C (JmjC) domain-containing enzymes.[12] The JmjC KDMs are Fe(II)/2-oxoglutarate (2OG)-dependent oxygenases.[15,16] Like other 2OG oxygenases, the JmjC domain in KDMs has a characteristic double-stranded β-helix (DSBH) fold, which harbors the Fe(II) and cosubstrate (2OG) binding to the enzyme's active site.[17−19] The active site of the KDMs contains conserved facial triad residues (Asp/Glu-X-His_2) binding to the Fe(II) center as in many other 2OG oxygenases.[20,21] Residues forming the JmjC domain and its surroundings are involved in substrate reorganization and substrate binding to the active site.[16,22,23]

KDM2A is the first known JmjC demethylase (Figure S1), identified specifically to demethylase lower (monomethylated and demethylated) methylation states of histone H3 lysine 36 (H3K36me1 and H3K36me2) to formaldehyde and succinate.[13,24] KDM2A is found in the nucleus and is expressed in several tissues, especially in the brain, lungs, ovaries, and testis, and it is also involved in the alternative lengthening of telomeres.[25−27] Altered KDM2A gene expression affects several cancers, significantly in lung, breast, and ovarian cancer;[6,26,28−32] therefore, the enzyme is a target for drug design. The overall catalytic mechanism of KDM2A is similar to other KDMs and other Fe(II)/2OG enzymes; the reaction starts with binding dioxygen to the Fe·2OG·substrate complex

Received: April 3, 2024
Revised: April 26, 2024
Accepted: April 30, 2024
Published: May 23, 2024

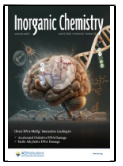

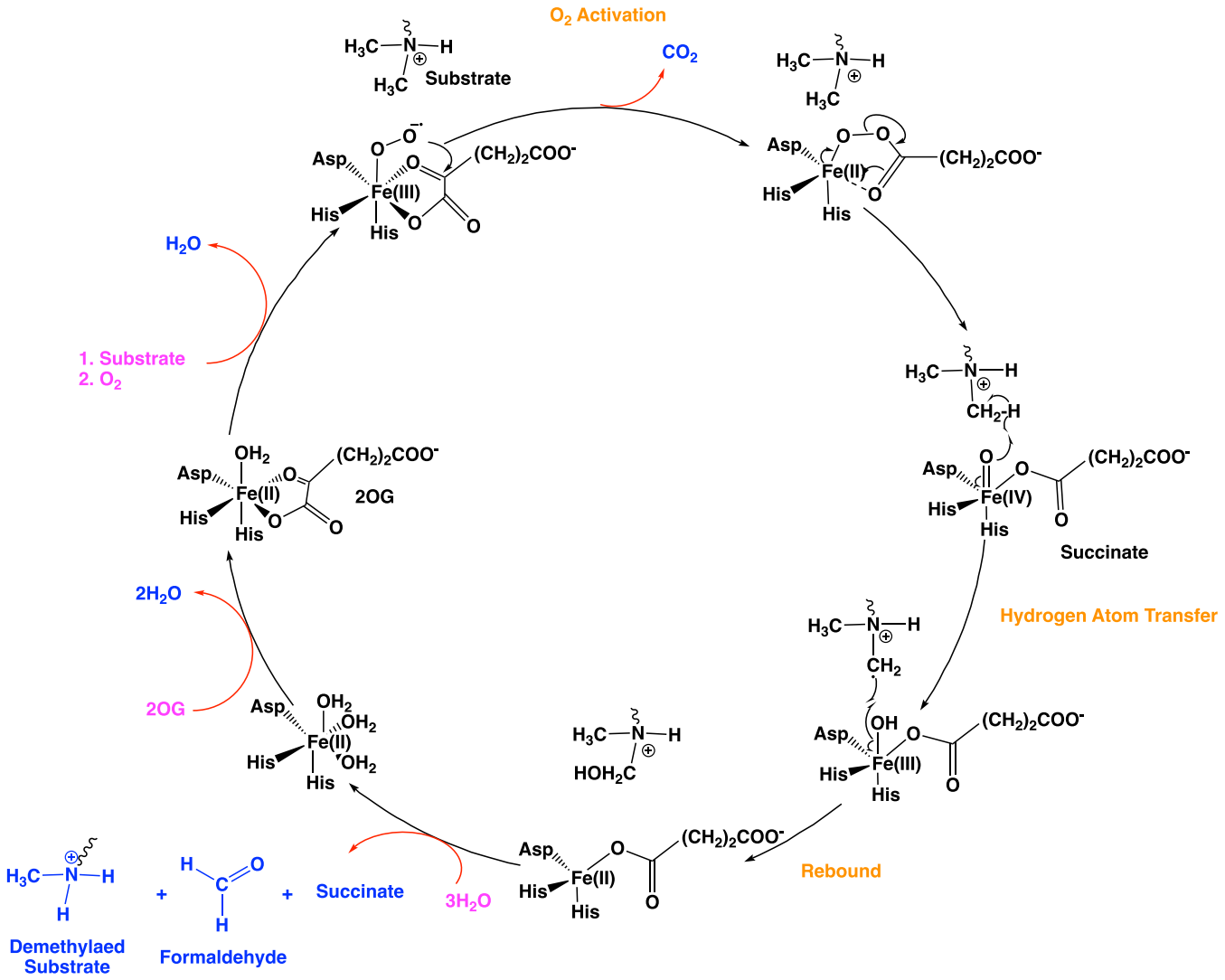

Figure 1. General catalytic mechanism of KDMs.

to form a ferric Fe(III)-superoxo complex.[33−37] The reaction proceeds through the oxidative decarboxylation of 2OG to form succinate and ferryl Fe(IV)═O intermediates. Then, the hydrogen atom abstraction (HAT) from the substrate by the ferryl results in substrate radical and ferric hydroxo Fe(III)−OH intermediate formation. Subsequent rebound hydroxylation forms a hemiaminal, followed by nonenzymatic elimination of formaldehyde and the demethylated product (Figure 1).

Crystallographic studies of KDM2A demonstrated that all three methylation states of H3K36 bind to KDM2A. However, it is interesting that the demethylation reaction is more effective for H3K36me2 than H3K36me1, and no demethylation activity is observed for H3K36me3.[38] As with some, but not all, other Fe(II)/2OG oxygenases,[36,39−42] experimental studies have illustrated that in KDM2A, a transition from off-line (with KDM2A, this involves coordination of 2OG C1 carboxylate trans to H284) binding mode to an in-line (with KDM2A, coordination of 2OG trans to H212) binding mode is necessary for the demethylation reaction (Figure S2).[38] The importance of such a transition from off-line to in-line 2OG coordination mode for effective catalysis has been demonstrated in PHF8 (KDM7B), showing 40% sequence similarity with KDM2A- and DNA-modifying enzymes AlkB and ALKBH2.[36,41] The importance of the off-line/in-line 2OG coordination modes has also been demonstrated in the catalysis of other Fe(II)/2OG enzymes such as halogenases[43,44] and EFE.[39,45,46] A recent study on another Fe-dependent enzyme, HgIS, highlights the importance of active site conformation and the rearrangement of the iron center for the C−H bond activation.[47] Therefore, understanding such conformational changes in the active site and Fe center rearrangements might have implications on the catalytic mechanism of other nonheme Fe(II) enzymes.

Notably, the crystallographic analysis of KDM2A shows evidence for changes in the conformation of the side chain of Y222 (Figure S2). Although the equivalent residue of Y222 in PHF8 is again a tyrosine residue (Y257), there is no evidence of conformational change. In the KDM2A·2OG·substrate complex, the phenolic hydroxyl group of Y222 points toward the metal center in the crystal structure, with off-line 2OG coordinated to Fe(II).[38] In contrast, in the crystal structure bound to *N*-oxalylglycine (NOG), the hydroxyl group is pointed toward the C5 carboxylate group of NOG.[38] Subsequently, these orientations of the Y222 side chain are referred to as off-line and in-line, respectively (Figure S2). The binding nitrogen oxide (used as an analogue of O_2, PDB ID: 4TN7) to the Fe(II) center of KDM2A manifests the in-line

https://doi.org/10.1021/acs.inorgchem.4c01365
Inorg. Chem. 2024, 63, 10737−10755

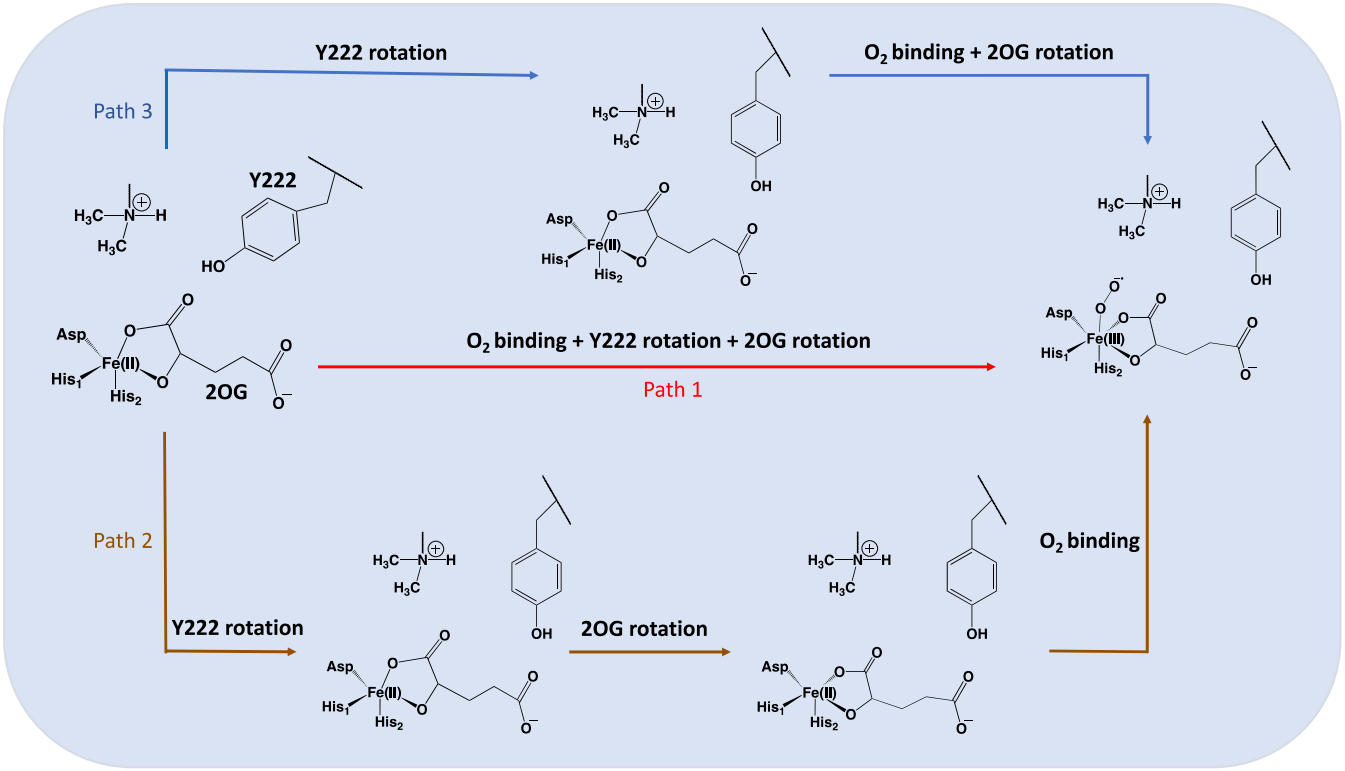

Figure 2. Possible pathways pertaining to the conformational changes involving Y222 and the coordination mode of 2-oxoglutarate (2OG). Here, His_1 is H212, His_2 is H284, and Asp is D214.

mode for 2OG and Y222.[38] The detailed mechanistic implication of the different crystallographically observed orientations of Y222 and 2OG, however, remains unknown (Figure 2).

A central, usually rate-limiting, step in KDMs is the HAT reaction, which is a fundamental chemical reaction of great interest for basic science[48−50] and applications in organic synthesis,[48,51−53] where it is utilized for the activation of C−H bonds.[54,55] The HAT reactions catalyzed by enzymes[56−58] are of great interest because of their unique regioselectivity,[59−61] stereoselectivity,[62−64] their requirement for mild and nontoxic conditions,[65] and, importantly, the ability to be modulated and altered by SCS and long-range (LR) interactions.[37,66] Although the overall mechanism of KDMs has been studied, the specific SCS and LR interactions that drive the catalysis in KDM2A are entirely unexplored. Understanding the specific SCS and LR interactions in KDM2 that are not presented in other KDMs is vitally essential for providing the background design of KDM2-specific inhibitors that do not affect other KDMs.

Here, we report molecular dynamics (MD)-based quantum mechanics/molecular mechanics (QM/MM) studies on the catalytic mechanism of KDM2A, focusing on how the SCS and LR interactions and protein dynamics enable the dioxygen reaction at the Fe(II) center, as well as the dioxygen activation and the substrate oxidation steps. Energy decomposition analysis is employed to understand the role of the SCS residues that stabilize the TS of each reaction step of the mechanism. The results highlight the importance of SCS conformational changes during the catalysis, in particular those involving Y222, which control the 2OG coordination binding mode.

2. METHODOLOGY

2.1. System Preparation. Crystal structures of KDM2A bound to Ni, 2OG/NOG, and all three methylenation states of $H3_{(29-41)}K36$ with off-line 2OG and in-line NOG were obtained with PDB accession codes 4QXH, 4QXC, 4QXB, 4QWN, 4QX7, and 4QX8 (Figure 3A).[38] Missing residues from 364−450 in the C-terminal domain were modeled using SWISS-MODEL.[67] The modeling follows the replacement of the Ni(II) metal ion with Fe(II) and, where appropriate, NOG with 2OG using GaussView 6.0 since Ni(II) and NOG were used for the crystallization. Protonation states of ionized residues were determined using Amber routines.[68] Metal Center Parameter Builder (MCPB.py) was used to generate parameters for the active site residues where Fe(II) is bound by two histidines, one aspartic acid residue, and bidentate 2OG/monodentate succinate.[69] The Antechamber module was used to parametrize nonstandard residues, such as methylated lysine (substrate) and 2OG/succinate.[70] Missing hydrogens and counterions were incorporated using the leap module of Amber 18.[71] The protein was subjected to solvation using a TIP3P water model extending 15 Å from the protein's surface.[72] The same method was executed to generate parameters for the ferric-superoxo and ferryl complexes. For the generation of all parameters, the active site was modeled to contain high-spin metal ions with spin (S) = 2 and multiplicity (M) = 5, as other experimental and computational studies reported.[73−78] Parameters for the remaining residues were generated using Amber FF14SB force field.[79]

2.2. Classical Molecular Dynamics (MD) Simulation. The simulations employed periodic boundary conditions. The particle mesh Ewald method was used to calculate long-range electrostatic and van der Waals interactions, with a cutoff of 10 Å.[80] The system minimization occurred in two stages. In the

https://doi.org/10.1021/acs.inorgchem.4c01365
Inorg. Chem. 2024, 63, 10737−10755

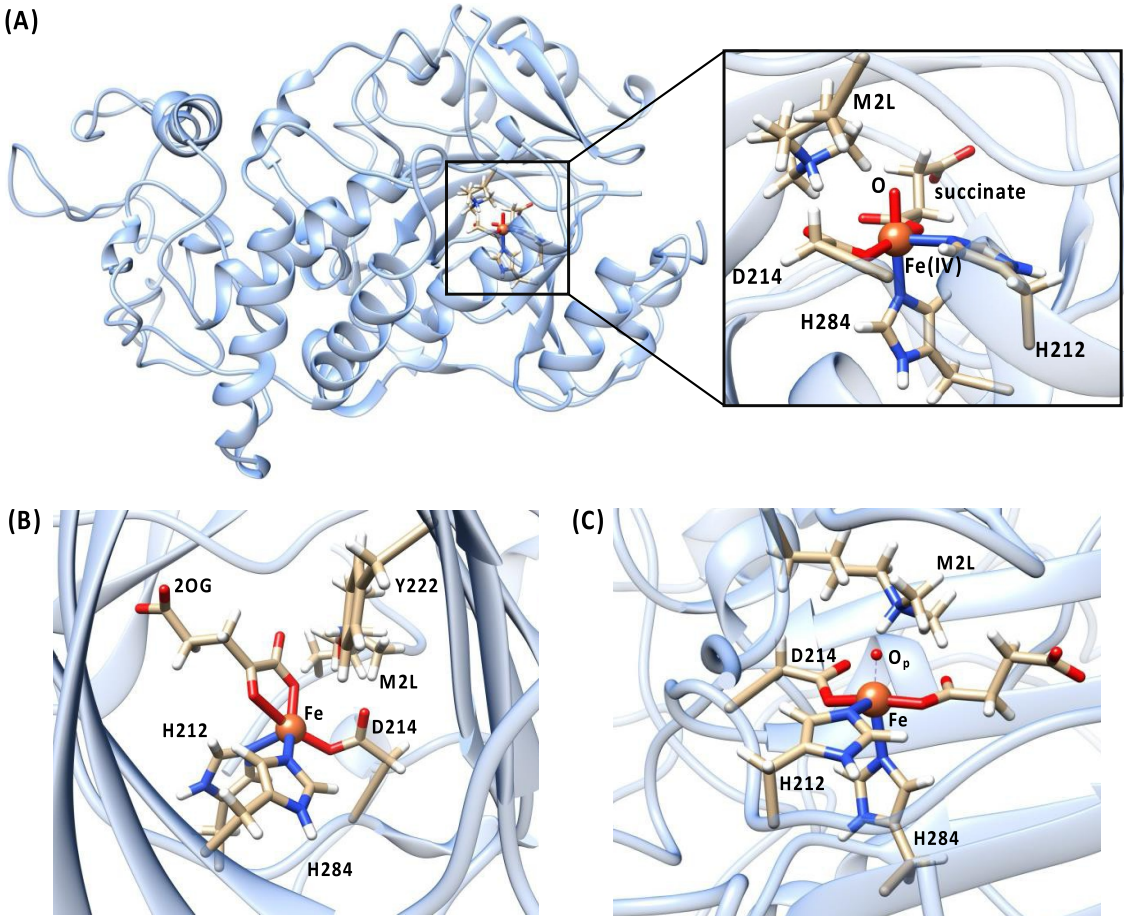

Figure 3. View of KDM2A. (A) View of the crystallographically derived structure of the enzyme KDM2A·H3K36·me2. The active site is zoomed. (B) View of the QM region residues for the QM/MM simulation of the ES complex of KDM2A·H3K36·me2. (C) View of the QM residues for the QM/MM calculations of the ferryl complex. Here, M2L represents dimethylated lysine.

first stage, solvent molecules were minimized for 10,000 steps, utilizing 5000 steps of steepest descent and 5000 steps of conjugate gradients while maintaining a 100 kcal/mol Å^2 constraint. The second minimization involved 10,000 steps without any constraints. Subsequently, the minimized system was subjected to controlled heating from 0 to 300 K using an NVT ensemble and a Langevin thermostat, with a heating period of 300 ps.[81] The system was then heated at a constant temperature of 300 K for 650 ps in an NPT ensemble, where the solute was subjected to a harmonic potential of 10 kcal/mol Å^2. The system was then equilibrated for 3 ns at a constant temperature of 300 K and a pressure of 1 bar. During the production MD phase, the system was simulated for 1 μs in an NPT ensemble, maintaining a pressure of 1 bar using the Berendsen barostat.[82] Bonds involving hydrogen atoms were constrained by utilizing the Shake algorithm.[83]

MD simulations were analyzed using various visualizing software, which is discussed in the Supporting Information (SI) (page S9). Root-mean-square deviation (RMSD) with respect to the equilibrated structure, root-mean-square fluctuation (RMSF), the radius of gyration (RoG), and the solvent accessible surface area (SASA) for the trajectories are given in the SI (Figures S3−S9).

2.3. Dioxygen Diffusion Dynamics. The diffusion pathway of dioxygen in KDM2A was studied by running a 1 μs MD simulation in the presence of dioxygen. The solvent box incorporated 100 dioxygen molecules to increase the probability of dioxygen diffusion to the active site.[84−86] Similarly, other computational studies have used similarly higher dioxygen concentrations (100 molecules).[84] Dioxygen molecules were randomly distributed across the solvent box using PACKMOL software.[87] Diffusion dynamics were performed with a similar protocol used in MD simulation. VMD was used to manually examine the diffusion of dioxygen.[88] Further, the diffusion pathway was characterized using CAVER 3.0 software.[89]

2.4. QM/MM Calculations. Snapshots obtained from MD simulations were used to perform QM/MM calculations using the ChemShell software package.[90] ChemShell software comprises Turbomole[91] and DL_POLY,[92] where Turbomole was used for the QM region, and DL_POLY was used for the MM region. Interactions between the QM and MM regions due to the polarization of the QM region by the charge distribution arising from the MM region were evaluated using an electronic embedding scheme.[93] The QM region comprises a nonheme Fe center, first coordination sphere residues (H212, H284, D214, and 2OG/succinate), and the substrate, as shown in Figure 3B. For the calculations involving 2OG and Y222 rearrangements, the QM region incorporated Y222 (Figure 3B). QM/MM calculations involving dioxygen-derived oxygen(s) in the active site were part of the QM region, i.e., at dioxygen binding, O_2 activation, HAT, and rebound stages (Figure 3C). The MM region contained residues within 8 Å of the QM region residues; the QM region is relaxed and the

https://doi.org/10.1021/acs.inorgchem.4c01365
Inorg. Chem. 2024, 63, 10737−10755

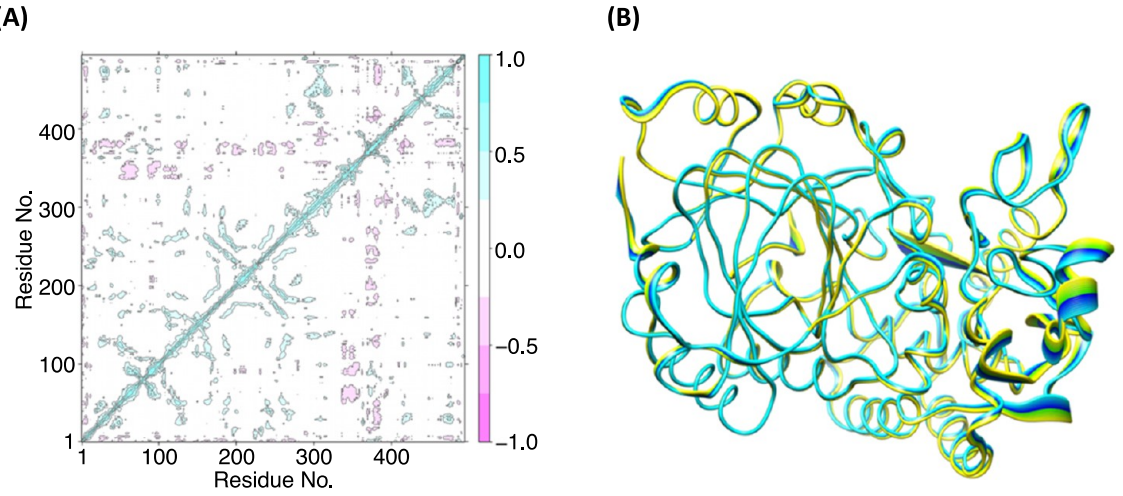

Figure 4. DCCA and PCA of the ES complex of KDM2A·H3K36·me2. (A) Residue numbers are as follows: Residues 1−482 (protein), 483 (Fe), 484 (2OG), and the remaining is the histone peptide (substrate). Cyan indicates positively correlated motions, and pink indicates negatively correlated motions. (B) A color gradient from blue to yellow indicates the direction of motion in the flexible regions of the enzyme. DCCA and PCA of KDM2A·H3K36·me1/me2 are provided in Figures S21 and S22.

regions outside the MM region are kept fixed. Hydrogens were used to link QM and MM regions. As in other similarly studied 2OG oxygenases, the QM region was treated with the unrestricted B3LYP functional[94] and the MM region with the Amber force field.[79] Both experimental and computational studies have consistently identified the quintet state (S = 2) as the ground spin state for nonheme enzymes.[74,95,96] Investigations into dioxygen activation and substrate oxidation studies across various nonheme enzymes have consistently demonstrated that the reaction proceeds through the HS quintet spin state (S = 2, M = 5).[97−99] Consequently, all mechanistic studies from dioxygen activation were conducted at the quintet spin state. Previous studies have also indicated that dioxygen binding occurs in the septet state.[86,100] Therefore, the QM/MM study involving dioxygen binding was performed at a septet state (S = 3, M = 7). Geometry optimization is followed by a relaxed potential energy surface (PES) scan with gradually changing reaction coordinates. The QM portion was optimized utilizing an m3 density functional theory (DFT) integration grid, with energies and gradients converging to 10^{-6} and 10^{-3} au, respectively.[101] Default approximations in the integral evaluations provided by Turbomole were utilized for the study. The DFT integration grid in Turbomole includes the quadrature of the exchange-correlation terms. The m3 integration grid employs the multigrid, which allows the gradient evaluation during the SCF iteration and reduces the computational cost without compromising the accuracy.[102] The highest energy point structure for transition state (TS) optimization was captured and optimized using a dimer method. Frequency calculations were used to characterize all formed minima and TS. All optimization and scans were performed using the DL-find optimizer implemented in the ChemShell package.[103] Optimizations were performed using a def2-SVP basis set and labeled as B1.[104,105] The choice of the basis set was made in alignment with previous computational studies on other KDMs[35−37,66,106] and many similar nonheme enzymes.[47,107−111] Energies were recalculated for better accuracy using a higher basis set def2-TZVP (B2 level of energy).[105] Zero-point energy calculations were performed for all optimizations and labeled as B3 (QM(B2 + ZPE)/MM). The accuracy of the results was investigated by using (i) an MM region of 6 and 10 Å, (ii) an expanded QM region, and (iii) D3 Grimme's dispersion correction for the HAT step, and results are provided in the SI (Table S1). To assess spin contamination in various systems (reactants and intermediates), the total spin $\langle S^2 \rangle$ was compared against $S \times (S + 1)$ (Table S2).[46,112] Substantial spin contamination is observed in structures involving antiferromagnetic coupling (the Fe(III)-superoxo complex) and the structure with the substrate radical, i.e., the Fe(III)-hydroxo complex, consistent with computational studies of similar nonheme enzymes.[46,113,114]

3. RESULTS AND DISCUSSION

3.1. Conformational Flexibility and Interactions in the ES Complexes of KDM2A. The nature of 5-coordinate (5C) KDM2A·Fe(II)·2OG·H3K36·me1/me2/me3 must control their different reactivities with dioxygen. Crystallographic studies provide important but static and averaged structural information that ignores significant conformational changes[115−118] which may affect the reactivity with dioxygen. To study these, we initiated 1 μs MD simulations for KDM2A bound to all three H3K36 methylation states (me1, me2, and me3 represent MD simulations of the ES complex of KDM2A·H3K36·me1/me2/me3, respectively). In me1 and me2, Y222 is aligned off-line with its hydroxyl group pointing toward the metal center. The C5 carboxylate in 2OG makes hydrogen bonding interactions with T209 and K229 (Figure S10). In contrast to me1 and me2, the MD simulation of me3 was performed using the crystal structure having off-line 2OG and in-line Y222 (Figure S10). Herein, the C5 carboxylate of 2OG interacts with T209, K229, and Y222. The off/in-line orientation of 2OG is measured along the dihedral angle N_{H212}−Fe−O2−O1 (N is the nitrogen of H212, and O1 and O2 are the two coordinating oxygens of 2OG, Figure S11) and is depicted in Figure S12. Similarly, the off/in-line orientation of the side chain of Y222 is measured by the dihedral angle to C−C_α−C_β−CZ (Figure S11) of Y222, as shown in Figure S13. To compare the orientation of Y257 in PHF8 with Y222 in KDM2A, we utilized previous MD simulations of PHF8 with off-line 2OG and in-line Y257.[86] The analysis demonstrates similar trends to that of KDM2A with off-line 2OG and in-line

https://doi.org/10.1021/acs.inorgchem.4c01365
Inorg. Chem. 2024, 63, 10737−10755

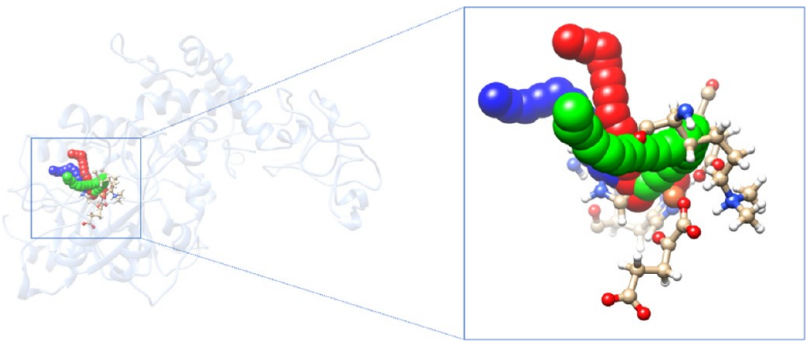

Figure 5. Possible dioxygen diffusion tunnels obtained from diffusion dynamics.

Y222 (me3), where the average distance between C5 of 2OG and hydroxyl hydrogen of Y222/257 is 3.19/3.03 Å (Figure S14), respectively, implying that in-line Y222 orientation is important in stabilizing 2OG and might aid the switching of 2OG coordination from off-line to in-line in PHF8 and KDM2A through its interaction with C5 oxygens of 2OG. However, there is no evidence for the conformational change of Y257 in PHF8. The non-Fe(II) coordinating oxygen of D214 makes stable hydrogen bonds with N298 in me2. In contrast with me1 and me3, the noncoordinating carboxylate oxygen is directed toward the substrate methyl group; it also interacts with the hydroxyl group of off-line Y222 in me1. Synergetic interactions between D214 and N298 may be crucial in substrate orientation (Figure S15).

Multiple hydrogen bonds of the histone H3 peptide with the backbone and side chains of KDM2A stabilize the substrate orientation in all methylation states, as in the crystal structures of KDM2A.[38] Residues H3A31, H3G33, H3G34, and H3 V35 comprise the N-terminal segment before methylated K36 and interact with the residues I188, N186, Y199, and K323, respectively. The C-terminal of the bound peptide (H3K37, H3P38, H3H39, and H3R40) contains large side chains accommodated within the enzyme cavity (Figure S16). The substrate is positioned in a hydrophobic sheath formed by the residues Y199, I144, L201, and F215 in all methylation states of KDM2A (Figure S17). Further, the S145 side chain interacts with the backbone carbonyl oxygen of K36. Significantly, an interaction of the ammonium hydrogen of H3K36 with N298 largely influences the direction of methylated ammonium toward the Fe(II) center. In me2, it forms 58% hydrogen bonding, while in me1, it is 25%, and this interaction is absent in me3 due to the lack of ammonium hydrogen (Figure S15). Overall, analysis of the hydrogen bonding interactions shows a better orientation for catalysis in KDM2A·H3K36·me2 than in H3K36·me1/me3 (Figures S18 and S19).

Dynamic cross-correlation analysis (DCCA) was performed in KDM2A·H3K36·me2 to explore the LR correlated motions with the active site and SCS residues (Figure 4A). Fe(II)-coordinating D214 and substrate-interacting F215 show an intense correlated motion with the region of the JmjC domain formed by β_{13}, α_{14}, α_{15}, α_{16}, and the loop connecting them (residues 292 to 346, the secondary structure elements of KDM2A are provided in Figure S20); this correlated motion might influence the substrate orientation. Additionally, the synchronized (positive correlation) motion of substrate-interacting residues I144, Y199, L201, and N298 with the region constituting β_5, α_7, α_8, and the loop connecting them might also influence the substrate orientation. A part of the C-terminal loop (residues 365−449) shows an intense negative correlation with the remaining region of the protein. Principal component analysis (PCA) (Figure 4B) shows that the C-terminal loop shows intense flexibility, whereas the rest of the protein shows minimal flexibility. Further, to elucidate the motion of the C-terminal loop in KDM2A·H3K36·me1/me3, DCCA, and PCA were performed, which show similar correlated motions and flexibility for the C-terminal loop to that of the KDM2A·H3K36·me2 complex (Figures S21 and S22).

3.2. Dioxygen Transport in KDM2A-H3K36me2. MD simulation (1 μs) to study the dioxygen diffusion in KDM2A·H3K36·me2 shows three tunnels for dioxygen diffusion, with an availability higher than 0.5−0.73, 0.69, and 0.57, respectively, shown in blue, green, and red (Figure 5). Several residues including I144, L201, T209, D210, F211, V213, V220, Y222, F231, I278, W282, I283, A285, and V286 are shared by the 3 tunnels (Figure S23). H3 residues H3G34, H3V35, H3K37, and H3P38 form a part of the red tunnel, whereas H3K37 and H3P38 form a part of the green tunnel. Dioxygen diffusion studies with PHF8·H3K9·me2 again show that histone peptides form a part of the dioxygen transport tunnels.[86] Therefore, the histone peptide chain in KDMs might play a key role in directing the dioxygen to form a productive reactive complex. MD trajectories revealed that all 3 tunnels are characterized with similar probability for the dioxygen transport from the exterior of the enzyme to the Fe(II) center. In all 3 tunnels, the dioxygen will approach the active site in an in-line fashion (opposite to H284), and only one dioxygen crossed over 2OG for a final off-line approach, as observed in the PHF8 enzyme (Figure S24).[86] During the crossover, dioxygen interacts with the hydrophobic residues I144, L201, Y222, and V294. Finally, the off-line approaching (trans to H212) dioxygen became trapped in a hydrophobic cage formed by the residues Y222, F231, F276, I278, and V286 for 700 ns (Figure S25). In the simulation, eight dioxygen molecules approached in an in-line fashion. Each remained in the Fe(II) center vicinity between 98.7, 40.9, 68.2, 34.5, 73.7, 91.1, and 69.4 ns. All eight dioxygens remained in the active site for 476 ns in total. The orientations of the side chains of K36me2, H3P38, I144, T209, and F215 facilitate the in-line approach of dioxygen toward the active site. Further, we compared the residence time for the dioxygen molecule in the active site of KDM2A with a similar study on α/β-hydrolase.[119] The study on α/β-hydrolase showed that the mean residence time for the oxygen molecule was 2.61 ns.[119] The difference in residence times was observed due to several factors. Primarily, it is the volume of the region for which the residential time in the different studies is calculated. Our study

https://doi.org/10.1021/acs.inorgchem.4c01365
Inorg. Chem. 2024, 63, 10737−10755

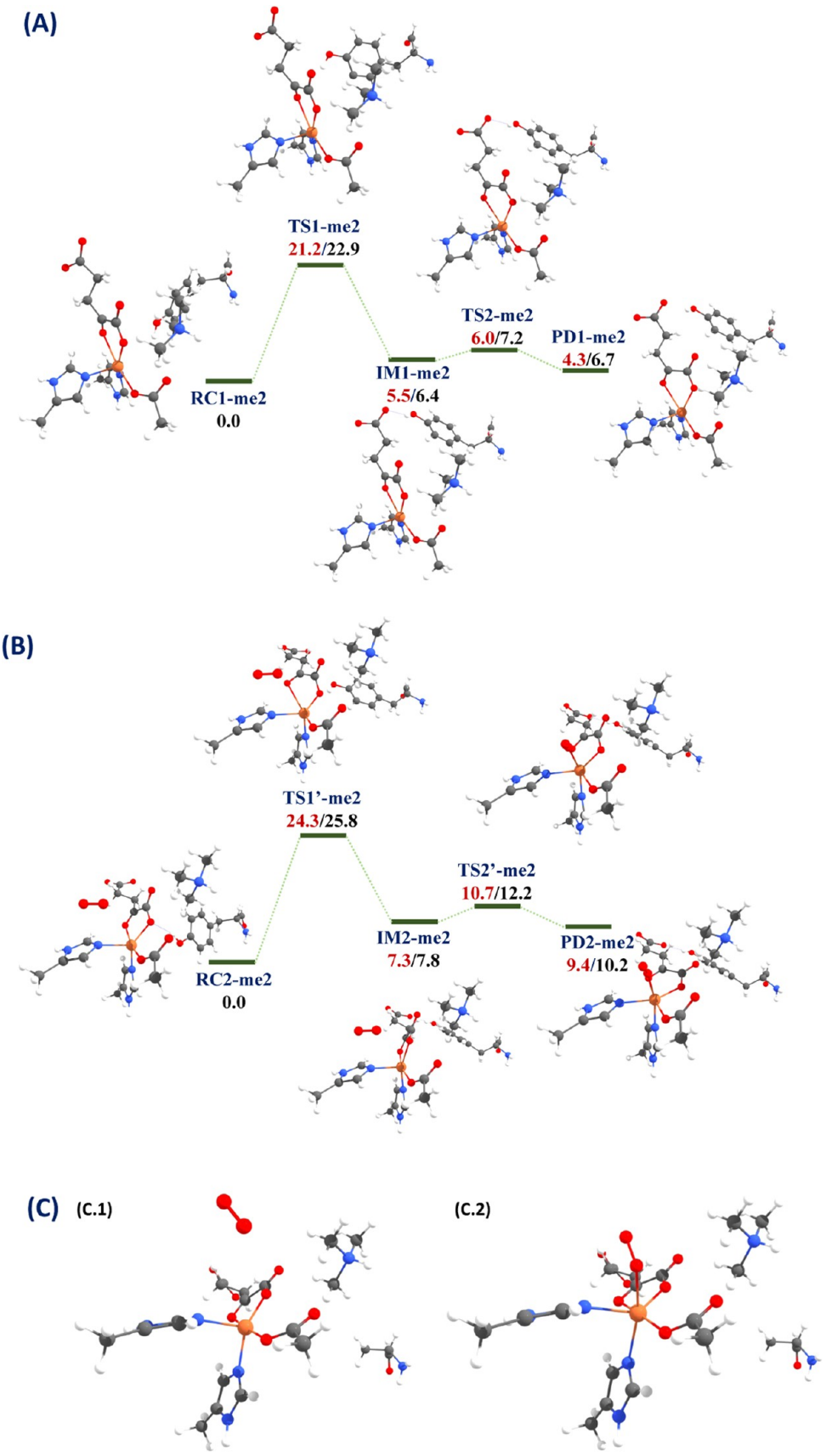

Figure 6. QM/MM potential energy profiles. (A) Potential energy surface for the 2OG and residue Y222 rearrangement in the absence of dioxygen. (B) Potential energy surface for the 2OG and residue Y222 rearrangement in the presence of dioxygen. (C) Image depicting dioxygen binding in the mutant Y222A: (C.1) unbound state and (C.2) bound state. Energies are provided in kcal/mol at UB3LYP/def2-TZVP (red) and with ZPE (black).

https://doi.org/10.1021/acs.inorgchem.4c01365
Inorg. Chem. 2024, 63, 10737−10755

analyzed the dioxygen molecules located in a sphere with a volume of 523 Å^3 centered at the Fe(II) center (radius of 5 Å), while in the study of α/β-hydrolase, the volume was much smaller (−15 Å^3). In addition, the number of dioxygen molecules varies in the two studies. After considering the two factors, the residential times in both studies become comparable. Another study on AlkB by Cisneros calculated the residential time by considering the distance between the Fe(II) and oxygen molecules (to be lower than 6 Å), also indicating about comparable residential times.[84] Further, the protein environment encompassing the region under investigation might contribute to residence times. In the present study, the off-line located dioxygen is a unique case; here, the in-line approaching dioxygen crossed over 2OG to become off-line-oriented, eventually being trapped in the highly hydrophobic cage formed by the residues Y222, F231, F276, I278, and V286 (Figure S25) without a direct exit tunnel, resulting in a high residence time. Thus, dioxygen transport studies indicate that the in-line dioxygen approach is preferred, a proposal that further requires 2OG rearrangement to form the catalytically productive in-line Fe(III)−OO$^{\bullet-}$ complex.

3.3. Mechanism of Dioxygen Binding. *3.3.1. Can the Fe(II) Center Undergo 2OG Rearrangement from Unproductive Off-Line to Productive In-Line Coordination Mode without the Binding of Dioxygen?* The dioxygen transport studies and structural inspection of the Fe(II) center imply that the rearrangement of off-line to in-line 2OG is necessary for productive catalysis. Furthermore, the crystal structure of KDM2A·Ni(II)·NO·NOG·H3K36me1 (PDB ID: 4TN7) shows the in-line orientations of both Y222 and NOG (Figure S26).[38] Here, we explore the mechanism of this 2OG rearrangement aiming to elucidate: (i) if the rearrangement of 2OG from off-line to in-line coordination mode happens before or during the binding of dioxygen; (ii) if the change of the orientation of the side chain of Y222 is a necessary requirement for the reorientation of 2OG to a productive coordination mode (Figure 2); and (iii) if the methylation status of H3K36 influences the 2OG rearrangement.

3.3.1.1. Can the 2OG Switch from Off-Line to In-Line Occur with the Off-Line Orientation of Y222? To explore the rearrangement of 2OG from off-line to in-line orientation without a change in the (off-line) position of the side chain of Y222, we performed the QM/MM potential energy surface (PES) calculations using the reaction coordinate as the change in the dihedral angle N_{H212}−Fe−O2−O1 (φ_1) (here, N is the nitrogen of H212, and O1 and O2 are the two coordinating oxygens of 2OG, Figure S11). A structure obtained from the MD simulation of KDM2A·H3K36·me2 was used as a starting structure for the QM/MM PES study. The bond distances between Fe(II) and the coordinating oxygens of 2OG in the chosen snapshot were 1.99 Å (Fe−O1) and 2.36 Å (Fe−O2). In the optimized geometry (RC-me2), these increased to 2.01 and 2.42 Å. The dihedral angle (φ_1) slightly decreased upon optimization from 113.2 to 110.2° in RC-me2. The calculated PES from RC-me2 leads to two minima with the corresponding values of the dihedral angle 139.9 and −171.7° with an energy barrier of ∼5 and ∼11 kcal/mol, respectively (Figure S27). The further 2OG rotation after the formation of the first minima increases the strain in the Fe−O2 bond and breaks it, forming the second minima where the torsion angle is flipped. Importantly, free optimization of both minima returned off-line 2OG orientation due to the steric hindering by the off-line positioned side chain of Y222 (Figure S26). Thus, the rearrangement of the 2OG coordination mode is not possible without a change in the orientation of the side chain of the SCS residue Y222.

3.3.1.2. How Does the Methylation Status of H3K36 Influence the 2OG Rearrangement? To further explore if the methylation status of H3K36 influences the 2OG rotation, we performed additional PES studies of the 2OG rearrangement using snapshots from the MD simulations of the H3K36me1 and H3K36me3 ES complexes of KDM2A. The me1 (RC-me1) ES complex possesses off-line 2OG and off-line Y222, whereas me3 (RC-me3) contains off-line 2OG; however, Y222 is in in-line coordination mode (Figure S10(C)). The PES calculation for the RC-me1 complex led to two minima with values for the torsion angle for φ_1 as 171.8 and −174.0°, respectively, with an energy barrier of ∼10 kcal/mol (Figure S28). The PES calculation starting from RC-me3 also led to two minima with values of φ_1 as 131.0 and 160.0° with an energy barrier of 10 and 15 kcal/mol, respectively. The free optimization of both minima in the RC-me1 scan led to an off-line 2OG coordination mode with an angle of 117.26°. For me3, despite the in-line orientation of Y222 in me3, the free optimization of the minima led again to off-line 2OG orientation (Figure S29). The instability of in-line 2OG in H3K36me3 is likely due to the substrate's bulky nature, which agrees with the experimental studies.[38,120]

Hence, the 2OG rearrangement studies with H3K36me1 and H3K36me2 show that the switch of the 2OG coordination mode from off-line to in-line cannot be achieved with Y222 in off-line orientation. The study with H3K36me3 shows that although Y222 is in in-line coordination, the bulky nature of the trimethylated K36 substrate prevents the 2OG rearrangement, which explains the experimental observation that KDM2A does not demethylase H3K36me3.[13,38]

3.3.1.3. Can the 2OG Switch be Realized with the In-Line Orientation of Y222? Taking into account that the 2OG rearrangement in the systems with the catalytically productive substrates H3K36me1 and H3K36me2 does not occur when Y222 is off-line-oriented, we further tested whether a change of Y222 from off-line to in-line will unlock the 2OG switch. We first performed a QM/MM potential energy scan to rotate off-line Y222 to the in-line orientation (Figure 6A). The PES was calculated using the reaction coordinate as the dihedral angle C−C_α−C_β−CZ in Y222 (φ_2) (Figure S11). The initial structure (RC1-me2) contained off-line orientations of 2OG and Y222 with the dihedrals φ_1 of 122.4° and φ_2 of 173.0°. The conversion of off-line Y222 to in-line mode requires an energy barrier of 22.9 kcal/mol (at the QM(B2 + ZPE)/MM level of theory) and is shown in Figure 6A. Free optimization of the product (IM1-me2) retained the in-line orientation of Y222. This conformation is stabilized by a strong hydrogen bonding between the hydroxyl group of Y222 and the C5 oxygens of 2OG (Figure 6A). We then used IM1-me2 to understand whether 2OG rearrangement can be achieved with in-line Y222. The QM/MM PES was calculated using the dihedral φ_1 from the IM1-me2 structure. The rotation of 2OG occurred virtually barrierless with ∼1 kcal/mol (Figure 6A) and the formed product minima (PD1-me2) show the formation of a partial in-line structure upon free optimization. The dihedral angle φ_1 in the optimized geometry (PD1-me2) was 141.6°, as observed in a previous computational study on PHF8.[36] Thus, the study shows that the transformation of the 2OG binding mode from off-line to in-line is possible for the catalytically productive substrates H3K36me1 and H3K36me2

https://doi.org/10.1021/acs.inorgchem.4c01365
Inorg. Chem. 2024, 63, 10737−10755

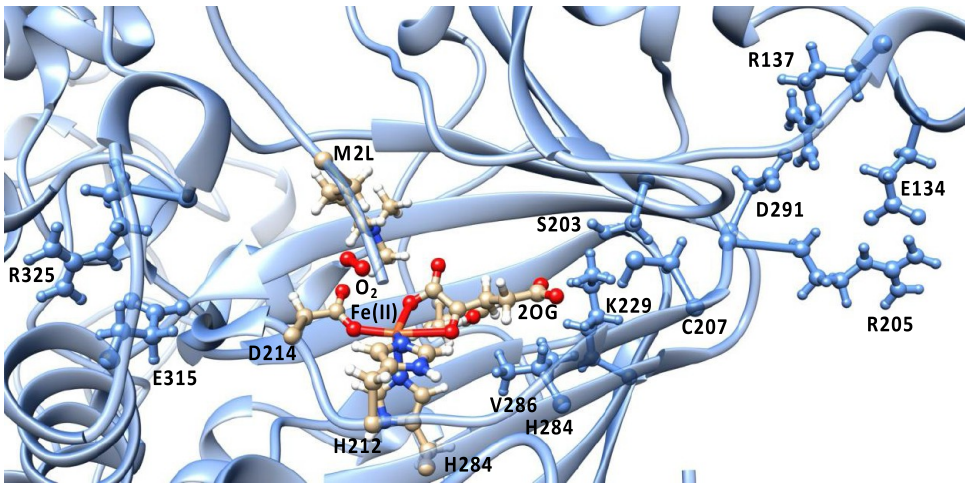

Figure 7. Residues shown in the blue ball and stick stabilize/destabilize TS5-me2 with respect to RC-me2 during the conformational change of Y222.

only when Y222 is in in-line mode. However, 2OG is not in complete in-line orientation in the optimized product.

3.3.2. What is the Reaction Mechanism of Dioxygen Binding, and Can It Induce the Rearrangement of 2OG and Y222 to Catalytically Productive Modes? Recent studies on the 2OG enzymes such as PHF8 and EFE demonstrate that dioxygen binding controls the binding mode of 2OG in their Fe(II) centers.[86] In order to evaluate if the binding of dioxygen can induce a switch in the orientation of Y222 and 2OG, we performed QM/MM calculations at the septet PES for the dioxygen binding to the Fe(II) center (Figure 2, Path 1). We selected a snapshot from the MD simulations of the dioxygen diffusion that represents an in-line approach of the dioxygen toward the Fe(II) center with an off-line orientation for both 2OG and Y222 and used the distance between Fe(II) and dioxygen as the reaction coordinate (Figure S24). The study shows that dioxygen binding to the Fe(II) center is highly unfavorable with off-line Y222 (Figure S30). This is primarily due to the steric constraints arising from the off-line orientation of Y222, specifically the steric clash between the off-line alignment of 2OG and Y222, which prevents the 2OG rearrangement and, ultimately the dioxygen binding (Figure S26). The results imply that the approaching dioxygen does not induce the reorientation of Y222 and should be completed before the process of dioxygen binding.

Then, we explored how the dioxygen binding to the Fe(II) center with off-line 2OG and already rotated to in-line mode Y222 takes place. A structure from the MD simulation of the dioxygen diffusion was QM/MM-optimized (RC2-me2) and used to rotate the side chain of Y222 from off-line to in-line in the presence of dioxygen. The energy barrier of this process is 25.8 kcal/mol (Figure 6B).

The free QM/MM-optimized structure with in-line Y222 (IM2-me2) was a further starting point to study the chemical binding of dioxygen to the Fe(II) center by decreasing the distance between Fe(II) and dioxygen with a decrement of 0.1 Å at the septet state as in previous studies.[46,86] The dioxygen binding triggers the rearrangement of 2OG from off-line to in-line in the presence of in-line Y222 to form an in-line ferric-superoxo Fe(III)−$OO^{\bullet-}$ intermediate. Free QM/MM optimization of the product led to the dioxygen unbinding at the septet spin state; however, a stable product (PD2-me2) was formed at the quintet spin state, which agrees with previous computational studies.[35,46,73,86] PD-me2 is stabilized by methylated lysine H3K36me2 and the SCS residue I144 (Figure S31). The energy barrier for the dioxygen binding coupled with 2OG rearrangement is 4.4 kcal/mol (Figure 2, Path 3). A similar energy barrier was observed for the in-line approach of dioxygen in PHF8 to form the Fe(III)−$OO^{\bullet-}$ complex, and the barrier was 6 kcal/mol.[86] Results were validated by performing a reverse scan on the in-line superoxo complex and are provided in the SI (Pages S36−S37 and Figure S32). The transition from the septet to the quintet state during the formation of the Fe(III)-superoxo complex proceeds via a spin-flip, as demonstrated in the previous computational studies of similar nonheme enzymes.[100,121]

To understand the role of protein residues affecting (lowering or increasing) the transition state for the rate-limiting step of the dioxygen binding (the conformational transition of Y222 from off-line to in-line), we performed energy decomposition analysis (EDA).[122,123] The results revealed that residues R137, R205, C207, K229, V286, and E315 stabilize, whereas E134, S203, D291, and R325 destabilize the transition state of this process (Figures 7 and S33). Importantly, K229, a residue that forms a hydrogen bonding interaction with the C5 carboxylate of 2OG, stabilizes the rearrangement by 6 kcal/mol, revealing the key role of the SCS residues in the process. The results show that dioxygen binding activates the 2OG rearrangement but not Y222, which should occur first. The conformational change in Y222 is a critical preliminary step for dioxygen to bind to the Fe(II) center to form the Fe(III)−$OO^{\bullet-}$ intermediate, in agreement with the crystallographic and mutagenesis studies.[38]

Notably, the role of the residue Y222 in the catalytic reaction of KDM2A was further explored by mutating the residue Y222 to alanine (Figures 6C and S34). These QM/MM studies with the Y222A variant demonstrated that 2OG rotation from off-line to in-line is barrierless, indicating the vital gatekeeping role of Y222 for this vital step in KDM2A catalysis.

Overall, our studies show that three factors are important for productive dioxygen binding. One is the methylation status of lysine, the second factor is the orientation of SCS Y222, and the third factor is the coordination mode of 2OG to Fe(II). Our study demonstrates the interdependence of these three factors.

https://doi.org/10.1021/acs.inorgchem.4c01365
Inorg. Chem. 2024, 63, 10737−10755

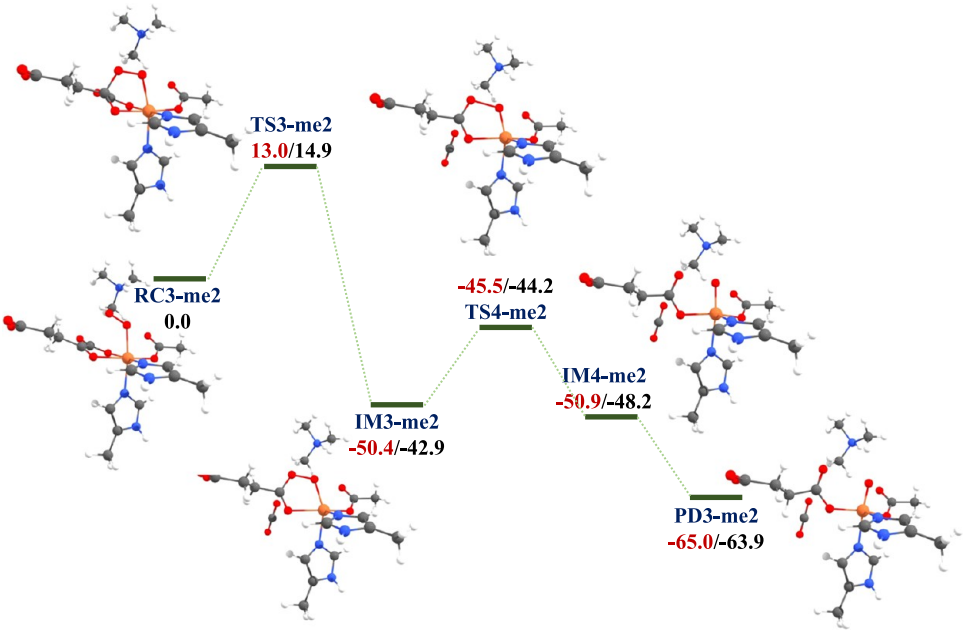

Figure 8. Potential energy surface for the dioxygen activation in KDM2A·H3K36·me2. Energies are provided in kcal/mol at UB3LYP/def2-TZVP (red) and with ZPE (black).

3.4. How Do the Flexibility and Interactions in In-Line Fe(III)-Superoxo Complexes Differ from the ES Complex? MD simulation is performed for 1 μs to study the dynamics of the in-line superoxo intermediate, thereby understating the influence of the bound dioxygen in the enzyme structure of KDM2A with mono (me1-SO) and dimethylated (me2-SO) substrates. Time-dependent fluctuation in the dihedral angles (ϕ1 and ϕ2) measuring the conformations of 2OG and Y222 demonstrates the in-line conformations of 2OG and Y222 in the superoxo complex, as shown in the crystal structure (Figures S35 and S36). Although central hydrogen bonding interactions are the same as in the ES complex, there is a change in the magnitude of these bonding interactions. These differences and specific interactions that stabilize the substrate and Fe-bound 2OG in the superoxo complexes are further discussed in the SI (Pages S42 to 43 and Figure S37).

DCCA and PCA are performed to understand the correlated motions in the superoxo complex (Figures S38 and S39) in comparison to the ES complex. The correlated motions present in the ES complex are also conserved in the superoxo complex. Further, residues of the JmjC domain that interact with the active site residues form a region utilizing β_9, β_{10}, α_{12}, α_{13}, and the loop connecting them. This region shows intense anticorrelated motion with α_4, α_5, α_7, and α_8 in me2-SO and not in me1-SO, which may influence the productive active site conformation. PCA of me1/me2-SO shows greater flexibility for the C-terminal, as demonstrated in the ES complex. Additionally, α_4 and α_5 in me2-SO show greater flexibility toward the active site, and this might influence the enzyme activity.

3.5. Reaction Mechanism of the O_2 Activation for Converting the In-Line Fe(III)-Superoxo to the In-Line Fe(IV)=O Complex. We further performed a mechanistic study to understand the reaction mechanism for the O_2 activation from the in-line KDM2A·Fe(III)−$OO^{\bullet-}$ intermediate with mono- and dimethylated substrates obtained from the MD simulations. The QM/MM-optimized geometry of the Fe(III)-superoxo complex with the dimethylated substrate (RC3-me2) shows Fe−O_p and O_p−O_d (O_p: proximal oxygen and O_d: distal oxygen) distances as 2.06 and 1.28 Å, respectively (Figure S40). The mechanism begins with the decarboxylation process, where the O_d of the dioxygen attacks C2 carbon to form a succinyl-peroxide intermediate (IM3-me2). The activation energy for the decarboxylation reaction is 14.9 kcal/mol, making it the rate-determining step (RDS) within the O_2 activation. The formation of IM3-me2 is highly exothermic (−42.93 kcal/mol), possibly due to the release of carbon dioxide to form succinate, similar to other FE(II)/2OG enzymes.[36,37,41,73,97] Homolytic cleavage of the O_p−O_d bond in IM3-me2 forms the IM4-me2 intermediate. Formation of IM4-me2 is a low-energy process with an energy barrier of 4.85 kcal/mol (at the QM(B2)/MM level of theory); the inclusion of zero-point energy (ZPE) correction makes it barrierless. Then, the formed intermediate rearranges to break the partial bond between O_p and O_d to form an in-line ferryl complex (PD3-me2). Formed PD3-me2 is highly stable with −63.9 kcal/mol as the relative energy. The Fe−O_p distance (1.62 Å) in PD3-me2 corresponds to the in-line ferryl intermediate, further characterized by the spin density (3.06). The reaction energy for the O_2 activation process is −64.43 kcal/mol, which is highly exergonic. The QM/MM potential energy profile and optimized geometries of the stationary points in the O_2 activation process of KDM2A bound to H3K36me2 are provided in Figures 8 and S40. The O_2 activation process in KDM2A with monomethylated lysine manifests similar trends to that of dimethylated lysine (Pages S46−S47 and Figures S41 and S42). The activation energy barrier for the RDS in KDM2A·Fe(III)−$OO^{\bullet-}$ with monomethylated lysine is 10.80 kcal/mol (Figure S41). We further explored energetic contributions from the SCS for stabilizing the transition state using EDA.[66,124] Figures S43 and S44 show that few residues commonly stabilize and destabilize TS3-me1 and TS3-me2. Residues D109, I144, K229, and E315 stabilize the TS, while charged residues like D74, K323, R325, and histone lysine residues H3K37 destabilize the TS and are illustrated in Figure

https://doi.org/10.1021/acs.inorgchem.4c01365
Inorg. Chem. 2024, 63, 10737−10755

9. Correlated motions of the EDA residues revealed that the EDA-stabilizing residues make a synchronized motion with a few regions of the protein. For instance, D109 correlates with β_6, I144 correlates with β_{13}, and D210 correlates with β_9, α_{12}, α_{13}, β_{10}, and the loop connecting them. Although these EDA residues are commonly found to stabilize the TS during the dioxygen activation of mono- and dimethylated substrates, these correlated motions are present only in me2-SO and not in me1-SO, implying the possibility for the better production of active conformations in me2 for the oxidation process. DCCA shows that the EDA-stabilizing residue E215 positively correlates with the β sheets (β_{10-14}) of the JmjC domain in me1-SO and me2-SO; this correlated motion might be significant for the dioxygen activation process.

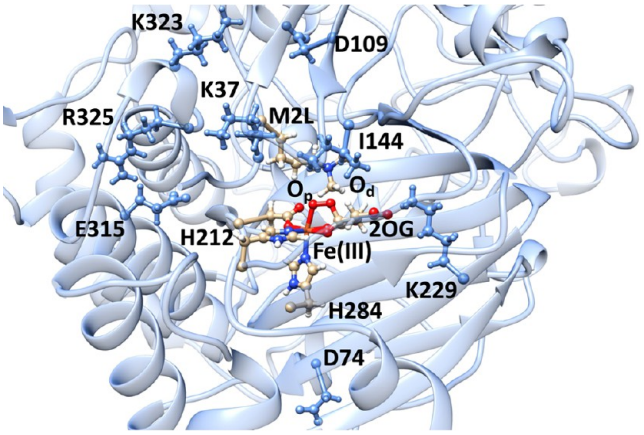

Figure 9. Residues shown in the blue ball and stick stabilize/destabilize TS3-me1 and TS5-me2 during the dioxygen activation.

3.6. What are the Interactions and Dynamics in the Fe(IV)=O Intermediate? The ferryl intermediate plays a vital role in the catalytic cycle of Fe(II)/2OG-dependent enzymes.[74] Experimental[125] and computational[126,127] studies on the 2OG-dependent enzymes have shown that the orientation of the C−H and Fe−O bonds influences the HAT reaction of substrate oxidation. Thus, 1 μs MD simulation was performed to understand the conformational dynamics of the in-line ferryl intermediate of KDM2A with mono- and dimethylated lysine (me1-ferryl and me2-ferryl). Experimental studies have shown that residues N298 and D214 might orient methylated K36 toward the Fe center; these interactions in the MD simulations are discussed in detail in the SI (Pages S51 and S52).[38] Therefore, we further measured the distances between ferryl oxygen and methylated carbons and between ferryl oxygen and nitrogen in me1-ferryl and me2-ferryl (Figures S45 and S46). In me2-ferryl, one of the methyl groups in dimethylated lysine points toward ferryl oxygen; however, another methyl group orients toward the residue

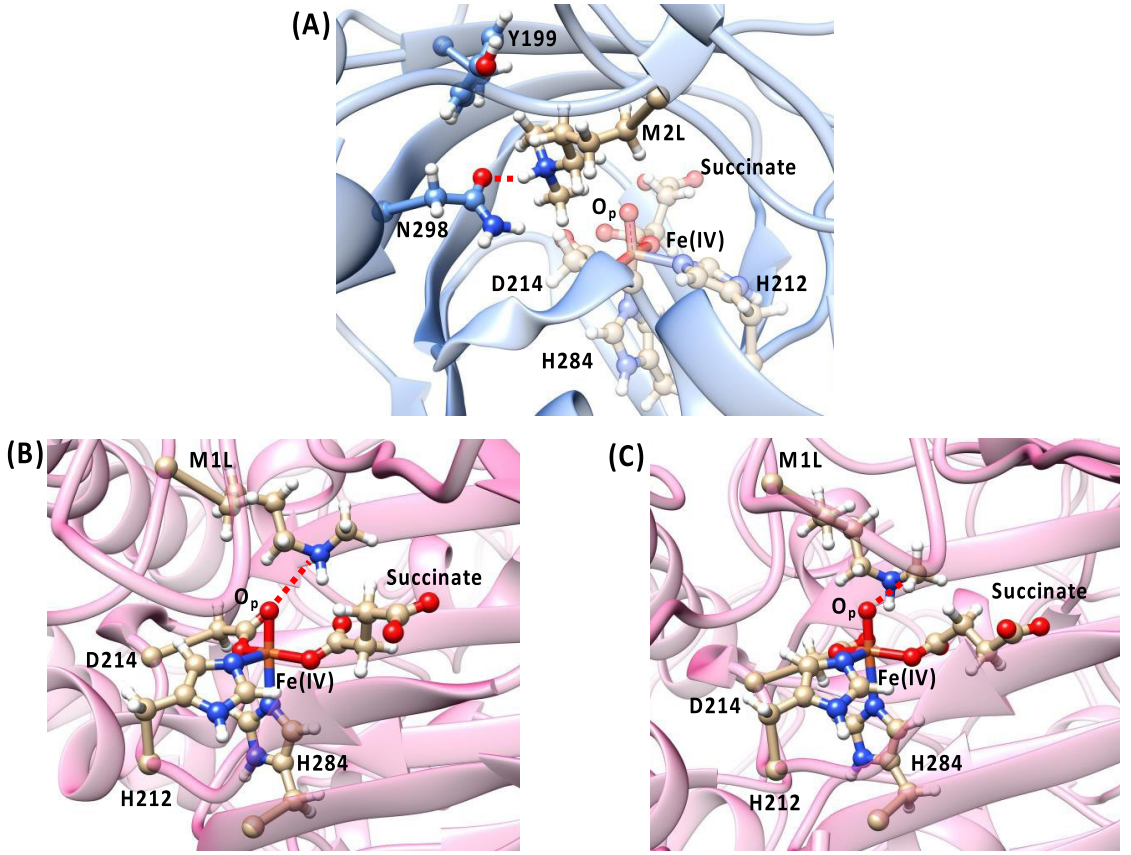

Figure 10. Conformation of the methyl group(s) in ferryl dynamics. (A) Strict orientation of the methyl groups in dimethylated lysine. One methyl group points toward the Fe center, and the other points toward Y199. The hydrogen bonding interaction between N298 and methylammonium hydrogen is shown in red. (B, C) Flexibility of the monomethylated group in the ferryl dynamics of KDM2A·H3K36·me1. (B) Methylammonium nitrogen points toward ferryl oxygen. (C) Methylated carbon points toward ferryl oxygen. Here, M1L and M2L represent monomethylated and dimethylated lysine.

https://doi.org/10.1021/acs.inorgchem.4c01365
Inorg. Chem. 2024, 63, 10737−10755

Y199. The strict orientation of the two methyl groups in dimethylated lysine arises from the hydrogen bond of methylammonium hydrogen with the residue N298 (Figures 10A and S47). Interestingly, in me1-ferryl, the methyl group accepts two orientations where nitrogen orients toward the metal center, while the other methyl group points away from the iron center, and the other orientation is the reverse of it (Figure 10B,C). Monomethylated lysine's flexibility may be due to its smaller size and the missing interaction between the methyl group and Y199. Cluster analysis along the MD trajectories confirmed the differential substrate orientations with mono/dimethylated lysine in KDM2A (Figure S48). DCCA and PCA of the ferryl complex show a similar trend to those of the ES complex and superoxo dynamics, as shown in Figures S49 and S50.

3.7. Mechanism of the Hydrogen Atom Transfer. To gain insights into the hydroxylation mechanism of KDM2A·Fe(IV)═O·H3K36me2, we perform QM/MM studies on multiple snapshots obtained from the MD of me2-ferryl. Hydroxylation is a two-step process, wherein the HAT reaction leads to rebound hydroxylation. During the HAT, the C−H bond on the substrate cleaves and binds with the ferryl oxygen; this involves electron transfer from the sigma C−H bond of the substrate to the 3d orbital of the Fe(IV) center. Previous studies have shown that electron transfer can occur via the σ or π channels.[36,37,66,78,128−134] σ transfer involves the transfer of the α electron from the substrate to the $\sigma^*_{z^2}$ of the metal, whereas π transfer involves the transfer of the β electron to the π^* orbitals of the metal, i.e., the π^*_{xz}/π^*_{yz}. Fe−O−H angle at the TS tends to correlate with the electron transfer pathway.[35−37,78,129,135] For the σ transfer of an electron, the Fe−O−H angle will be close to 180°, and for π transfer, the angle will be closer to 120°.[129,135] Analysis of the TS structure shows that in five snapshots, the Fe−O−H angle varies from 128 to 150°, suggesting a σ transfer of the electrons (Table S3). Essentially, the interaction of the residue I144 and the methyl group stabilizes this angle of the TS. Calculation of the spin density of the TS shows a negative spin density of the substrate carbon in all of the snapshots, confirming the σ transfer (Table S3). The HAT transition state's spin natural orbitals (SNOs) were calculated and are represented in Figure S51, confirming the σ transfer mechanism. Experimental and computational studies also show that frontier molecular orbitals (FMOs) involved in the HAT reactions are $\sigma^*_{z^2}$ and $\pi_{xz/yz}$.[37,66,78,111,129] Analysis of the MOs for all of the snapshots involved in the HAT also indicates a preference for $\sigma^*_{z^2}$ since $\sigma^*_{z^2}$ is the lowest unoccupied MO (LUMO). The LUMO is stabilized ∼3 kcal/mol to that of π^*_{xz} in all of the snapshots (Figure 11 and Table S4).

The potential energy surface for the HAT reaction is depicted in Figures 12 and 13. The Boltzmann average activation barrier from the five HAT reaction paths is 21.96 kcal/mol, with the lowest and highest values being 21.19 and 24.84 kcal/mol, which is comparable to the other computational studies of similar enzymes (Figure 13).[35−37,66,106] The reaction energy profile for the HAT process indicates that the intermediate (IM5-me2) is endothermic in all of the snapshots. The intermediate represents forming a Fe(III)−OH bond and a substrate radical (Table S5). The spin densities and Mulliken charges of the optimized geometries in the HAT are tabulated in Figure 14 and Tables S5 and S6. Additional calculations were performed using (i) different MM regions (6 and 10 Å), (ii) extended QM regions (including residues T209 and Y222,

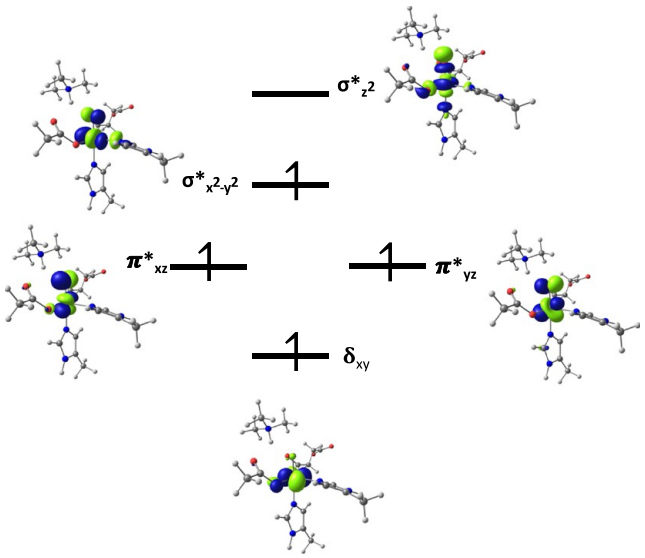

Figure 11. Frontier molecular orbitals of the Fe(IV)═O intermediate in KDM2A-H3K36me2.

Figure S52), and (iii) D3 dispersion correction to validate the results obtained in the HAT. All calculations show consistent activation and reaction energies, and the results are presented in Table S1.

SCS residues have been found to stabilize the HAT TSs[37,66,108,136,137] and were actively explored as a tool to alter enzyme activity and specificity.[138−140] In KDM2A, N298 forms a hydrogen bond with the hydrogen of methylated carbon pointed away from the metal center (Figure 15A). Additionally, the nonbonding oxygen of D214 makes hydrogen bonding interactions with dimethylamino hydrogen; the noncoordinating oxygen of succinate forms a hydrogen bonding interaction with the hydrogen of hydroxylating carbon in the substrate (Figure 15A). EDA of the lowest energy snapshot in the HAT reveals that the residues N142, D167, K229, and E315 mainly stabilize the TS, whereas residues D109, I144, R159, D291, and R325 destabilize TS5-me2 (Figures 15B and S53). Correlated motions of the EDA residues of the HAT reveal the strong positive correlations with the β-sheets and α-helixes of the JmjC domain (Figure S50). For instance, residues N142 and D167 show a correlation with β_6, β_7, α_{11}, β_8, β_{10}, and β_{13}, which might influence the orientation of the active site for the oxidative reaction. The TS-destabilizing MM residue I144 positively correlates with the residue N298, signifying the tight substrate orientation. Further, the correlated motions are much more intense in me2-ferryl than in me1-ferryl as in the superoxo dynamics, implying the role of correlated motions in the catalytic mechanism.

3.8. Rebound Hydroxylation. The rebound hydroxylation mechanism involves the transfer of OH^- from Fe(III)−OH to the substrate carbon radical. Herein, the hydroxyl group in IM5-me2 is transferred to the substrate radical to form a hydroxylated product (PD) by reducing Fe(III)−OH to Fe(II). Product formation is rapid and highly favorable since the energy barrier for the rebound mechanism is 1.4 kcal/mol, in parallel with the other computational studies (Figure 12).[107,141] The low energy barrier for the rebound reaction may be due to the hydrogen bonding interaction with succinate's noncoordinating oxygen with the hydroxyl group

https://doi.org/10.1021/acs.inorgchem.4c01365
Inorg. Chem. 2024, 63, 10737−10755

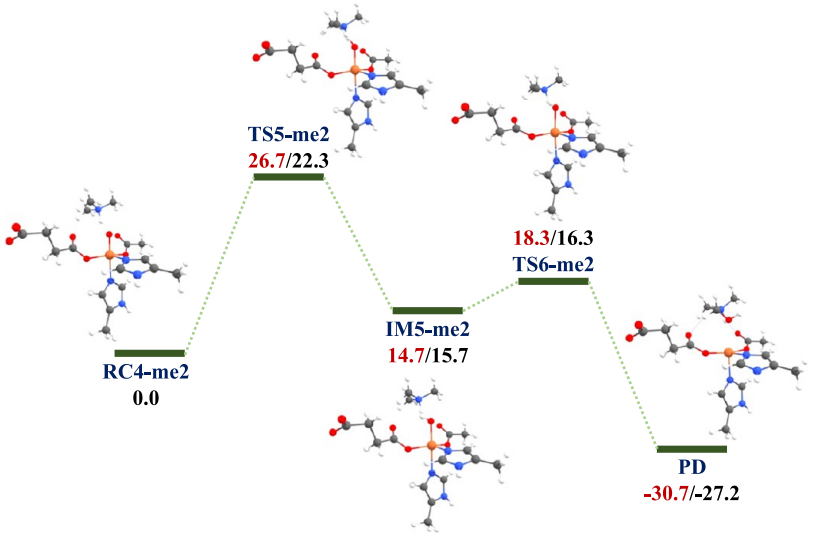

Figure 12. Potential energy surface for the HAT and rebound reaction in KDM2A-H3K36me2. Energies are provided in kcal/mol at UB3LYP/def2-TZVP (red) and with ZPE (black).

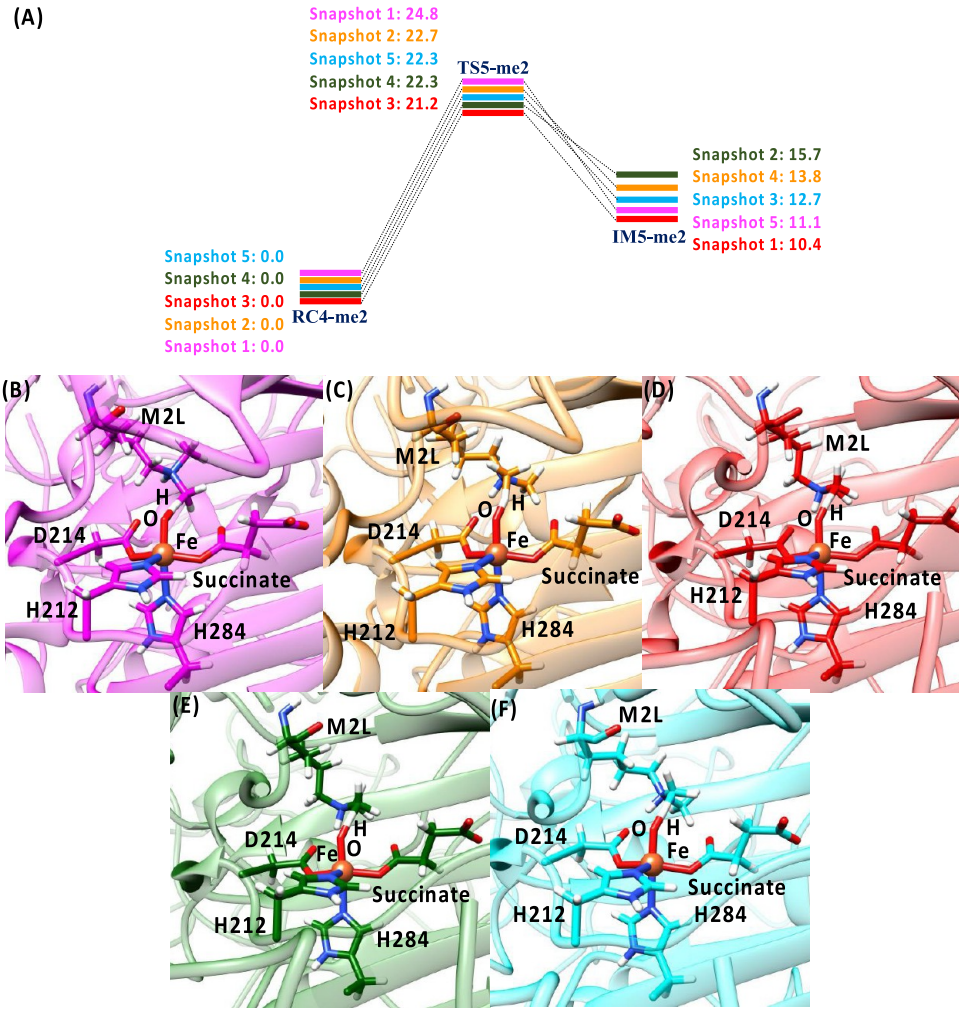

Figure 13. (A) Reaction profile of the HAT in KDM2A for the different snapshots. Energies are provided in kcal/mol at UB3LYP/def2-TZVP with ZPE corrections. QM/MM-optimized geometries of the HAT transition state. (B) Snapshot 1, (C) snapshot 2, (D) snapshot 3, (E) snapshot 4, and (F) snapshot 5. Key angles, spin density, and Mulliken charges are provided in Tables S3, S5, and S6. Here, M2L represents dimethylated lysine.

https://doi.org/10.1021/acs.inorgchem.4c01365
Inorg. Chem. 2024, 63, 10737−10755

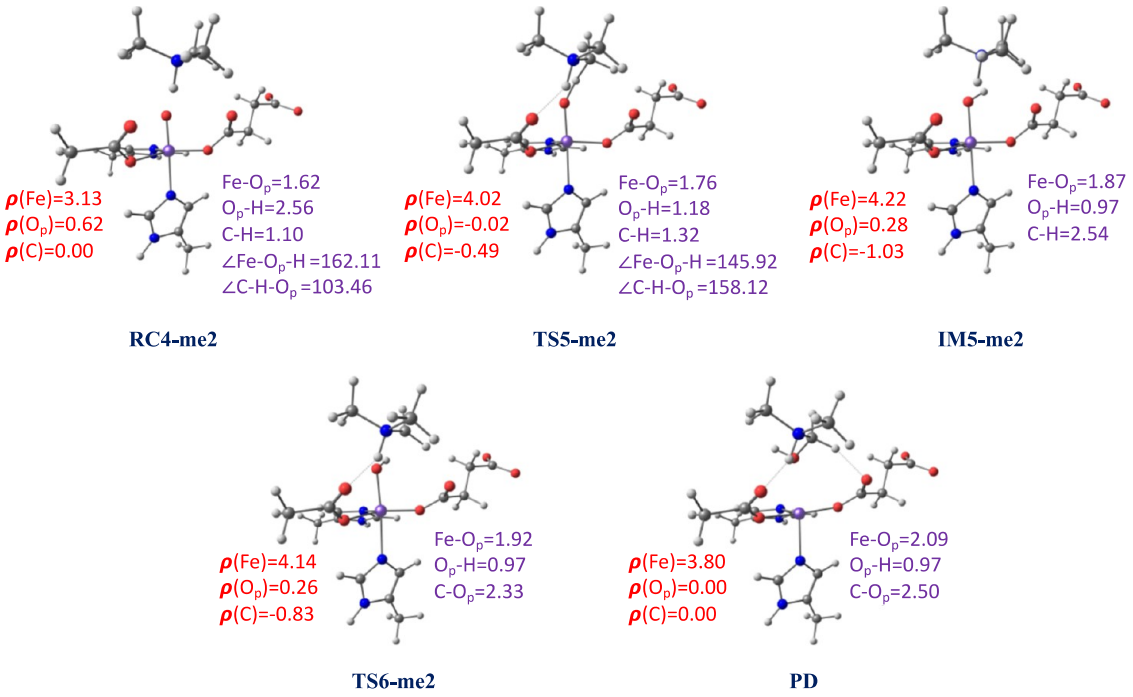

Figure 14. Optimized geometries of the stationary points during the HAT and rebound process in KDM2A·H3K36·me2. Distances and spin densities are shown in violet and red.

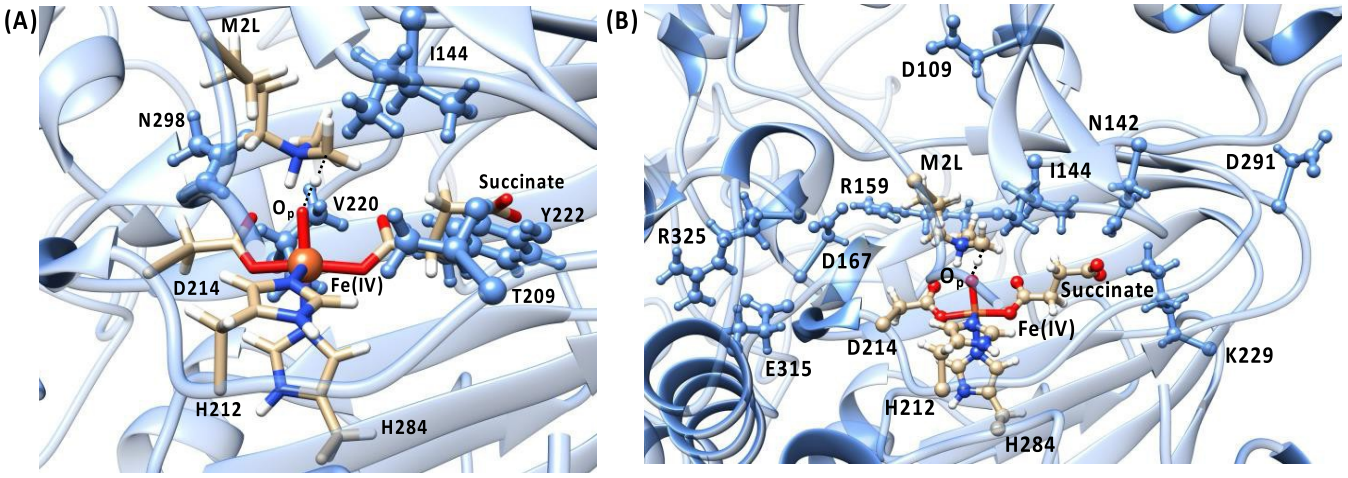

Figure 15. SCS interacting residues. (A) Sterically TS-stabilizing residues during the HAT reaction. (B) Residues (from EDA) shown in the blue ball and stick energetically stabilize/destabilize TS5-me2 with respect to RC4-me2 during the HAT. Here, M2L represents dimethylated lysine.

in IM1. The PD formed is highly exothermic, and the reaction energy is −42.35 kcal/mol. The PD is stabilized by the hydrogen bond of the substrate with the nonbonded oxygens of aspartate and succinate. Spin densities of the transition state and the product in the rebound reaction are consistent with the previous studies and are provided in Figure 14.[36,142,143] EDA analysis of the rebound transition state (TS6-me2 −IM5-me2) shows that residues N142, D167, and E315 stabilized the TS, whereas residues I144, R159, and D210 destabilized it (Figure S54). The correlated motions of these EDA residues are like those observed in the HAT.

3.9. Do the Same SCS Residues Stabilize the TSs of the Different Reaction Steps? A detailed comparison of the EDA at various catalytic steps reveals that few SCS residues significantly stabilize the TS structures. Residues K229 and E315 stabilize the TSs in all steps in the catalytic process, whereas R325 destabilizes them. Therefore, we performed QM/MM of the HAT step, additionally including the TS-stabilizing residues K229 and E315. The activation energy and reaction energy were found to be similar to that of the calculations with the standard QM region (Table S1). Interestingly, all MD simulations show that correlated motions of K229, E315, and R325 with the residues of the JmjC domain remain the same, signifying the role of long-range correlations in the catalytic mechanism. K229 plays a central role in stabilizing all catalytic steps, most significantly the conformational change of Y222 from off-line to in-line. EDA analysis reveals that the residue I144 plays a dual role in the dioxygen activation and the HAT and rebound process. During the dioxygen activation, the residue I144 stabilizes TS3-me1/me2, whereas it destabilizes TS5-me2 and TS6-me2 in the

https://doi.org/10.1021/acs.inorgchem.4c01365
Inorg. Chem. 2024, 63, 10737−10755

HAT and rebound process, illustrating the role of SCS residues in controlling the reaction mechanism.

To elucidate the role of SCS residues in stabilizing the TSs during the oxidation process in KDM2A, we compared them to the energetic contributions of the SCS residues in other KDMs such as KDM4A,[35] KDM6A/B,[37] and PHF8 (KDM7B).[36,66] The equivalent of the TS-stabilizing residue E315 in KDM2A is E350 in PHF8, which again shows TS stabilization. The other residues that stabilize the TS in PHF8 are Y265 and N279. Interestingly, the corresponding residue to K229 in KDM4A (K206) shows a similar hydrogen bonding interaction with the C5 carboxylate of 2OG. However, no identical residues stabilizing the active site or the TS during the oxidation reaction are found in KDM6. The observed correlated motions of the TS-stabilizing residues with the JmjC domain are also reflected in other KDMs, signifying the role of domain architecture in the catalytic process.

4. CONCLUSIONS

Our study utilized a series of MD-based QM/MM simulations to explore the catalytic mechanism of KDM2A. Like other 2OG oxygenases, KDM2A follows a general mechanism where the cosubstrate (2OG) and the substrate binding replace the water molecules to form a 5-coordinated ES complex. Dioxygen binds to the Fe(II) center in the ES complex, resulting in a Fe(III)-superoxo complex. The formed Fe(III)-superoxo complex then undergoes a decarboxylation reaction to form a ferryl complex and succinate. MD simulation of the ES complex of KDM2A·H3K36·me1/me2/me3 reveals fundamental hydrogen bonding interactions and correlated motions of the ES complex favoring the substrate orientation to the Fe(II) center.

Dioxygen transport simulations show that the tunnel-forming protein residues direct the dioxygen to the Fe(II) center and adequately orient the dioxygen in an in-line (trans to H284) fashion. QM/MM calculations show that forming the in-line ferric-superoxo complex from the 5-coordinated enzyme−substrate complex in KDM2A is unproductive without the change in the orientation of the side chain of the SCS residue Y222 and the change of the coordination mode of 2OG from off-line to in-line modes. The study demonstrated that the conformational change of the side chain of Y222 controls the formation of partial in-line geometry in K36me1 and K36me2; however, the bulkier nature of K36me3 prevents the 2OG rearrangement and, therefore, blocks the catalytic reaction at this stage.

The QM/MM study of the in-line binding of dioxygen to the Fe(II) center with in-line Y222 leads to the formation of the productive Fe(III)-superoxo complex. The QM/MM calculations of the Y222A variant showed that the 2OG rearrangement from off-line to in-line proceeds almost barrierless, thus confirming the role of Y222 to be a gatekeeper of the catalytic reaction.

Further, MD simulation of the ferryl complex demonstrated a preference for H3K36me2 over H3K36me1 because of the hydrogen bonding interaction with the SCS residue N298. QM/MM calculation of the HAT and rebound hydroxylation reactions in KDM2A·H3K36·me2 showed that the HAT proceeds via the σ transfer. The rebound pathway is energetically favored and requires a much lower activation energy compared to that of the HAT. EDA analysis coupled with DCCA shows that SCS residues K229, E315, and R325 play a vital role in the catalytic process and positively correlate with residues of the JmjC domain. Further, I144 plays a role in dioxygen activation and the HAT and rebound process, signifying the role of the SCS residue in the catalytic process. We believe that our study will contribute to understanding the complexity of the catalytic mechanisms of Fe(II)/2OG-dependent KDMs and will help identify better inhibitors for KDM2A that do not influence other KDMs and other Fe(II)/2OG enzymes.

■ ASSOCIATED CONTENT

Supporting Information

The Supporting Information is available free of charge at https://pubs.acs.org/doi/10.1021/acs.inorgchem.4c01365.

QM geometries of QM/MM-optimized structures; spin densities; Mulliken charges, and supporting data on QM/MM and MD results (PDF)

■ AUTHOR INFORMATION

Corresponding Author

Christo Z. Christov − *Department of Chemistry, Michigan Technological University, Houghton, Michigan 49931, United States;* orcid.org/0000-0002-4481-0246; Email: christov@mtu.edu

Authors

Midhun George Thomas − *Department of Chemistry, Michigan Technological University, Houghton, Michigan 49931, United States*

Simahudeen Bathir Jaber Sathik Rifayee − *Department of Chemistry, Michigan Technological University, Houghton, Michigan 49931, United States;* orcid.org/0000-0001-8557-078X

Shobhit S. Chaturvedi − *Department of Chemistry, Michigan Technological University, Houghton, Michigan 49931, United States;* orcid.org/0000-0003-4977-5600

Koteswara Rao Gorantla − *Department of Chemistry, Michigan Technological University, Houghton, Michigan 49931, United States;* orcid.org/0000-0003-4541-8796

Walter White − *Department of Chemistry, Michigan Technological University, Houghton, Michigan 49931, United States*

Jon Wildey − *Department of Chemical Engineering, Michigan Technological University, Houghton, Michigan 49931, United States*

Christopher J. Schofield − *Chemistry Research Laboratory, Department of Chemistry and the Ineos Oxford Institute for Antimicrobial Research, University of Oxford, Oxford OX1 5JJ, U.K.;* orcid.org/0000-0002-0290-6565

Complete contact information is available at: https://pubs.acs.org/10.1021/acs.inorgchem.4c01365

Notes

The authors declare no competing financial interest.

■ ACKNOWLEDGMENTS

This research was supported by the NIH/NIGMS grant 1R15GM139118-01A1 and in part by the Wellcome Trust (106244/Z/14/Z). For the purpose of open access, the authors have applied a CC BY4.0 public copyright license to any Author Accepted Manuscript version arising from this submission.

REFERENCES

(1) Sims, R. J.; Nishioka, K.; Reinberg, D. Histone Lysine Methylation: A Signature for Chromatin Function. *Trends Genet.* **2003**, *19* (11), 629−639.

(2) Chi, P.; Allis, C. D.; Wang, G. G. Covalent Histone Modifications—Miswritten, Misinterpreted and Mis-Erased in Human Cancers. *Nat. Rev. Cancer* **2010**, *10* (7), 457−469.

(3) Pedersen, M. T.; Helin, K. Histone Demethylases in Development and Disease. *Trends Cell Biol.* **2010**, *20* (11), 662−671.

(4) Wang, G. G.; Allis, C. D. Misinterpretation" of a Histone Mark Is Linked to Aberrant Stem Cells and Cancer Development. *Cell Cycle* **2009**, *8* (13), 1979−1983.

(5) Ooi, W. F.; Yao, X.; Tan, P.; Teh, B. T. Misregulation of Histone Methylation Regulators in Cancer. In *DNA and Histone Methylation as Cancer Targets*; Kaneda, A.; Tsukada, Y., Eds.; Springer International Publishing: Cham, 2017; pp 221−248.

(6) Neganova, M. E.; Klochkov, S. G.; Aleksandrova, Y. R.; Aliev, G. Histone Modifications in Epigenetic Regulation of Cancer: Perspectives and Achieved Progress. *Semin. Cancer Biol.* **2022**, *83*, 452−471.

(7) Tian, X.; Fang, J. Current Perspectives on Histone Demethylases. *Acta Biochim. Biophys. Sin.* **2007**, *39* (2), 81−88.

(8) Li, K. K.; Luo, C.; Wang, D.; Jiang, H.; Zheng, Y. G. Chemical and Biochemical Approaches in the Study of Histone Methylation and Demethylation. *Med. Res. Rev.* **2012**, *32* (4), 815−867.

(9) Marmorstein, R.; Trievel, R. C. Histone Modifying Enzymes: Structures, Mechanisms, and Specificities. *Biochim. Biophys. Acta, Gene Regul. Mech.* **2009**, *1789* (1), 58−68.

(10) Walport, L. J.; Hopkinson, R. J.; Chowdhury, R.; Schiller, R.; Ge, W.; Kawamura, A.; Schofield, C. J. Arginine Demethylation is Catalysed by a Subset of JmjC Histone Lysine Demethylases. *Nat. Commun.* **2016**, *7* (1), No. 11974.

(11) Shi, Y.; Lan, F.; Matson, C.; Mulligan, P.; Whetstine, J. R.; Cole, P. A.; Casero, R. A.; Shi, Y. Histone Demethylation Mediated by the Nuclear Amine Oxidase Homolog LSD1. *Cell* **2004**, *119* (7), 941−953.

(12) Rea, S.; Eisenhaber, F.; O'Carroll, D.; Strahl, B. D.; Sun, Z.-W.; Schmid, M.; Opravil, S.; Mechtler, K.; Ponting, C. P.; Allis, C. D.; Jenuwein, T. Regulation of Chromatin Structure by Site-Specific Histone H3Methyltransferases. *Nature* **2000**, *406* (6796), 593−599.

(13) Tsukada, Y.-i.; Fang, J.; Erdjument-Bromage, H.; Warren, M. E.; Borchers, C. H.; Tempst, P.; Zhang, Y. Histone Demethylation by a Family of JmjC Domain-Containing Proteins. *Nature* **2006**, *439* (7078), 811−816.

(14) Burg, J. M.; Link, J. E.; Morgan, B. S.; Heller, F. J.; Hargrove, A. E.; McCafferty, D. G. KDM1 Class Flavin-dependent Protein Lysine Demethylases. *Pept. Sci.* **2015**, *104* (4), 213−246.

(15) Jia, B.; Tang, K.; Chun, B. H.; Jeon, C. O. Large-Scale Examination of Functional and Sequence Diversity of 2-Oxoglutarate/Fe(II)-Dependent Oxygenases in Metazoa. *Biochim. Biophys. Acta, Gen. Subj.* **2017**, *1861* (11), 2922−2933.

(16) Markolovic, S.; Leissing, T. M.; Chowdhury, R.; Wilkins, S. E.; Lu, X.; Schofield, C. J. Structure−Function Relationships of Human JmjC Oxygenases—Demethylases versus Hydroxylases. *Curr. Opin. Struct. Biol.* **2016**, *41*, 62−72.

(17) McDonough, M. A.; Loenarz, C.; Chowdhury, R.; Clifton, I. J.; Schofield, C. J. Structural Studies on Human 2-Oxoglutarate Dependent Oxygenases. *Curr. Opin. Struct. Biol.* **2010**, *20* (6), 659−672.

(18) Aik, W.; McDonough, M. A.; Thalhammer, A.; Chowdhury, R.; Schofield, C. J. Role of the Jelly-Roll Fold in Substrate Binding by 2-Oxoglutarate Oxygenases. *Curr. Opin. Struct. Biol.* **2012**, *22* (6), 691−700.

(19) Markolovic, S.; Wilkins, S. E.; Schofield, C. J. Protein Hydroxylation Catalyzed by 2-Oxoglutarate-Dependent Oxygenases. *J. Biol. Chem.* **2015**, *290* (34), 20712−20722.

(20) Bruijnincx, P. C. A.; Van Koten, G.; Gebbink, R. J. M. K. Mononuclear Non-Heme Iron Enzymes with the 2-His-1-Carboxylate Facial Triad: Recent Developments in Enzymology and Modeling Studies. *Chem. Soc. Rev.* **2008**, *37* (12), 2716−2744.

(21) Hegg, E. L.; Q, L., Jr. The 2-His-1-Carboxylate Facial Triad - An Emerging Structural Motif in Mononuclear Non-Heme Iron(II) Enzymes. *Eur. J. Biochem.* **1997**, *250* (3), 625−629.

(22) Aik, W. S.; Chowdhury, R.; Clifton, I. J.; Hopkinson, R. J.; Leissing, T.; McDonough, M. A.; Nowak, R.; Schofield, C. J.; Walport, L. J. Introduction to Structural Studies on 2-Oxoglutarate-Dependent Oxygenases and Related Enzymes. In *2-Oxoglutarate-Dependent Oxygenases*; Schofield, C.; Hausinger, R., Eds.; The Royal Society of Chemistry, 2015; pp 59−94.

(23) Ng, S. S.; Kavanagh, K. L.; McDonough, M. A.; Butler, D.; Pilka, E. S.; Lienard, B. M. R.; Bray, J. E.; Savitsky, P.; Gileadi, O.; Von Delft, F.; Rose, N. R.; Offer, J.; Scheinost, J. C.; Borowski, T.; Sundstrom, M.; Schofield, C. J.; Oppermann, U. Crystal Structures of Histone Demethylase JMJD2A Reveal Basis for Substrate Specificity. *Nature* **2007**, *448* (7149), 87−91.

(24) Cheng, X.; Trievel, R. C. JmjC Lysine Demethylases. In *2-Oxoglutarate-Dependent Oxygenases*; Schofield, C.; Hausinger, R., Eds.; The Royal Society of Chemistry, 2015; pp 210−245.

(25) Frescas, D.; Guardavaccaro, D.; Kuchay, S. M.; Kato, H.; Poleshko, A.; Basrur, V.; Elenitoba-Johnson, K. S.; Katz, R. A.; Pagano, M. KDM2A Represses Transcription of Centromeric Satellite Repeats and Maintains the Heterochromatic State. *Cell Cycle* **2008**, *7* (22), 3539−3547.

(26) Liu, L.; Liu, J.; Lin, Q. Histone Demethylase KDM2A: Biological Functions and Clinical Values (Review). *Exp. Ther. Med.* **2021**, *22* (1), No. 723.

(27) Li, F.; Wang, Y.; Hwang, I.; Jang, J.-Y.; Xu, L.; Deng, Z.; Yu, E. Y.; Cai, Y.; Wu, C.; Han, Z.; Huang, Y.-H.; Huang, X.; Zhang, L.; Yao, J.; Lue, N. F.; Lieberman, P. M.; Ying, H.; Paik, J.; Zheng, H. Histone Demethylase KDM2A Is a Selective Vulnerability of Cancers Relying on Alternative Telomere Maintenance. *Nat. Commun.* **2023**, *14* (1), No. 1756.

(28) Lin, Q.; Wu, Z.; Yue, X.; Yu, X.; Wang, Z.; Song, X.; Xu, L.; He, Y.; Ge, Y.; Tan, S.; Wang, T.; Song, H.; Yuan, D.; Gong, Y.; Gao, L.; Liang, X.; Ma, C. ZHX2 Restricts Hepatocellular Carcinoma by Suppressing Stem Cell-like Traits through KDM2A-Mediated H3K36 Demethylation. *EBioMedicine* **2020**, *53*, No. 102676.

(29) Okamoto, K.; Tanaka, Y.; Ogasawara, S.; Obuse, C.; Nakayama, J.; Yano, H.; Tsuneoka, M. KDM2A-Dependent Reduction of rRNA Transcription on Glucose Starvation Requires HP1 in Cells, Including Triple-Negative Breast Cancer Cells. *Oncotarget* **2019**, *10* (46), 4743−4760.

(30) Song, Y.; Yang, G.; Ma, D.; Wang, W.; Leung, C. The Role and Prospect of Lysine-specific Demethylases in Cancer Chemoresistance. *Med. Res. Rev.* **2023**, *43* (5), 1438−1469.

(31) Dhar, S. S.; Alam, H.; Li, N.; Wagner, K. W.; Chung, J.; Ahn, Y. W.; Lee, M. G. Transcriptional Repression of Histone Deacetylase 3 by the Histone Demethylase KDM2A Is Coupled to Tumorigenicity of Lung Cancer Cells. *J. Biol. Chem.* **2014**, *289* (11), 7483−7496.

(32) Andricovich, J.; Tzatsos, A. Biological Functions of the KDM2 Family of Histone Demethylases. In *Targeting Lysine Demethylases in Cancer and Other Human Diseases*; Yan, Q., Ed.; Springer International Publishing: Cham, 2023; Vol. *1433*, pp 51−68.

(33) Hausinger, R. P. Fe(II)/α-Ketoglutarate-Dependent Hydroxylases and Related Enzymes. *Crit. Rev. Biochem. Mol. Biol.* **2004**, *39* (1), 21−68.

(34) Martinez, S.; Hausinger, R. P. Catalytic Mechanisms of Fe(II)- and 2-Oxoglutarate-Dependent Oxygenases. *J. Biol. Chem.* **2015**, *290* (34), 20702−20711.

(35) Ramanan, R.; Chaturvedi, S. S.; Lehnert, N.; Schofield, C. J.; Karabencheva-Christova, T. G.; Christov, C. Z. Catalysis by the JmjC Histone Demethylase KDM4A Integrates Substrate Dynamics, Correlated Motions and Molecular Orbital Control. *Chem. Sci.* **2020**, *11* (36), 9950−9961.

(36) Chaturvedi, S. S.; Ramanan, R.; Lehnert, N.; Schofield, C. J.; Karabencheva-Christova, T. G.; Christov, C. Z. Catalysis by the Non-Heme Iron(II) Histone Demethylase PHF8 Involves Iron Center

https://doi.org/10.1021/acs.inorgchem.4c01365
Inorg. Chem. 2024, 63, 10737−10755

Rearrangement and Conformational Modulation of Substrate Orientation. *ACS Catal.* **2020**, *10* (2), 1195−1209.
(37) Rifayee, S. B. J. S.; Chaturvedi, S. S.; Warner, C.; Wildey, J.; White, W.; Thompson, M.; Schofield, C. J.; Christov, C. Z. Catalysis by KDM6 Histone Demethylases − A Synergy between the Non-Heme Iron(II) Center, Second Coordination Sphere, and Long-Range Interactions. *Chem. - Eur. J.* **2023**, *29* (51), No. e202301305.
(38) Cheng, Z.; Cheung, P.; Kuo, A. J.; Yukl, E. T.; Wilmot, C. M.; Gozani, O.; Patel, D. J. A Molecular Threading Mechanism Underlies Jumonji Lysine Demethylase KDM2A Regulation of Methylated H3K36. *Genes Dev.* **2014**, *28* (16), 1758−1771.
(39) Chaturvedi, S. S.; Ramanan, R.; Hu, J.; Hausinger, R. P.; Christov, C. Z. Atomic and Electronic Structure Determinants Distinguish between Ethylene Formation and L -Arginine Hydroxylation Reaction Mechanisms in the Ethylene-Forming Enzyme. *ACS Catal.* **2021**, *11* (3), 1578−1592.
(40) Zhang, Z.; Ren, J.; Harlos, K.; McKinnon, C. H.; Clifton, I. J.; Schofield, C. J. Crystal Structure of a Clavaminate Synthase−Fe(II)−2-oxoglutarate−Substrate−NO Complex: Evidence for Metal Centred Rearrangements. *FEBS Lett.* **2002**, *517* (1−3), 7−12.
(41) Waheed, S. O.; Ramanan, R.; Chaturvedi, S. S.; Lehnert, N.; Schofield, C. J.; Christov, C. Z.; Karabencheva-Christova, T. G. Role of Structural Dynamics in Selectivity and Mechanism of Non-Heme Fe(II) and 2-Oxoglutarate-Dependent Oxygenases Involved in DNA Repair. *ACS Cent. Sci.* **2020**, *6* (5), 795−814.
(42) Tang, H.; Wu, M.-H.; Lin, H.-Y.; Han, M.-R.; Tu, Y.-H.; Yang, Z.-J.; Chien, T.-C.; Chan, N.-L.; Chang, W. Mechanistic Analysis of Carbon−Carbon Bond Formation by Deoxypodophyllotoxin Synthase. *Proc. Natl. Acad. Sci. U.S.A.* **2022**, *119* (1), No. e2113770119.
(43) Vennelakanti, V.; Li, G. L.; Kulik, H. J. Why Nonheme Iron Halogenases Do Not Fluorinate C−H Bonds: A Computational Investigation. *Inorg. Chem.* **2023**, *62* (48), 19758−19770.
(44) Vennelakanti, V.; Mehmood, R.; Kulik, H. J. Are Vanadium Intermediates Suitable Mimics in Non-Heme Iron Enzymes? An Electronic Structure Analysis. *ACS Catal.* **2022**, *12* (9), 5489−5501.
(45) Yeh, C.-C. G.; Ghafoor, S.; Satpathy, J. K.; Mokkawes, T.; Sastri, C. V.; De Visser, S. P. Cluster Model Study into the Catalytic Mechanism of α-Ketoglutarate Biodegradation by the Ethylene-Forming Enzyme Reveals Structural Differences with Nonheme Iron Hydroxylases. *ACS Catal.* **2022**, *12* (7), 3923−3937.
(46) Xue, J.; Lu, J.; Lai, W. Mechanistic Insights into a Non-Heme 2-Oxoglutarate-Dependent Ethylene-Forming Enzyme: Selectivity of Ethylene-Formation *versus* L -Arg Hydroxylation. *Phys. Chem. Chem. Phys.* **2019**, *21* (19), 9957−9968.
(47) Fu, Y.; Wang, B.; Cao, Z. Coordination Dynamics of Iron Center Enables the C−H Bond Activation: QM/MM Insight into the Catalysis of Hydroxyglutarate Synthase (HglS). *J. Catal.* **2023**, *428*, No. 115149.
(48) Wang, L.; Xiao, J. Hydrogen-Atom Transfer Reactions. In *Topics in Current Chemistry Collections*; Guillena, G.; Ramón, D. J., Eds.; Springer International Publishing: Cham, 2016; pp 205−259.
(49) Subramanian, H.; Sibi, M. P. Stereoselective Hydrogen Atom Transfer in Free Radical Reactions. *Asian J. Org. Chem.* **2023**, *12* (6), No. e202300175.
(50) Mayer, J. M. Understanding Hydrogen Atom Transfer: From Bond Strengths to Marcus Theory. *Acc. Chem. Res.* **2011**, *44* (1), 36−46.
(51) Wu, Z.-X.; Hu, G.-W.; Luan, Y.-X. Development of *N* -Hydroxy Catalysts for C−H Functionalization via Hydrogen Atom Transfer: Challenges and Opportunities. *ACS Catal.* **2022**, *12* (19), 11716−11733.
(52) Roberts, B. P. Polarity-Reversal Catalysis of Hydrogen-Atom Abstraction Reactions: Concepts and Applications in Organic Chemistry. *Chem. Soc. Rev.* **1999**, *28* (1), 25−35.
(53) Green, S. A.; Crossley, S. W. M.; Matos, J. L. M.; Vásquez-Céspedes, S.; Shevick, S. L.; Shenvi, R. A. The High Chemofidelity of Metal-Catalyzed Hydrogen Atom Transfer. *Acc. Chem. Res.* **2018**, *51* (11), 2628−2640.
(54) Crabtree, R. H.; Lei, A. Introduction: CH Activation. *Chem. Rev.* **2017**, *117* (13), 8481−8482.
(55) Capaldo, L.; Ravelli, D. Hydrogen Atom Transfer (HAT): A Versatile Strategy for Substrate Activation in Photocatalyzed Organic Synthesis. *Eur. J. Org. Chem.* **2017**, *2017* (15), 2056−2071.
(56) *Iron-Containing Enzymes: Versatile Catalysts of Hydroxylation Reactions in Nature*; De Visser, S. P.; Kumar, D., Eds.; Royal Society of Chemistry: Cambridge, 2011.
(57) Cheng, L.; Wang, H.; Cai, H.; Zhang, J.; Gong, X.; Han, W. Iron-Catalyzed Arene C−H Hydroxylation. *Science* **2021**, *374* (6563), 77−81.
(58) Gandeepan, P.; Müller, T.; Zell, D.; Cera, G.; Warratz, S.; Ackermann, L. 3d Transition Metals for C−H Activation. *Chem. Rev.* **2019**, *119* (4), 2192−2452.
(59) Wojdyla, Z.; Borowski, T. On How the Binding Cavity of AsqJ Dioxygenase Controls the Desaturation Reaction Regioselectivity: A QM/MM Study. *JBIC, J. Biol. Inorg. Chem.* **2018**, *23* (5), 795−808.
(60) Kluza, A.; Wojdyla, Z.; Mrugala, B.; Kurpiewska, K.; Porebski, P. J.; Niedzialkowska, E.; Minor, W.; Weiss, M. S.; Borowski, T. Regioselectivity of Hyoscyamine 6β-Hydroxylase-Catalysed Hydroxylation as Revealed by High-Resolution Structural Information and QM/MM Calculations. *Dalton Trans.* **2020**, *49* (14), 4454−4469.
(61) Wojdyla, Z.; Borowski, T. Properties of the Reactants and Their Interactions within and with the Enzyme Binding Cavity Determine Reaction Selectivities. The Case of Fe(II)/2-Oxoglutarate Dependent Enzymes. *Chem. - Eur. J.* **2022**, *28* (18), No. e202104106.
(62) Leveson-Gower, R. B.; Mayer, C.; Roelfes, G. The Importance of Catalytic Promiscuity for Enzyme Design and Evolution. *Nat. Rev. Chem.* **2019**, *3* (12), 687−705.
(63) Mai, B. K.; Neris, N. M.; Yang, Y.; Liu, P. C−N Bond Forming Radical Rebound Is the Enantioselectivity-Determining Step in P411-Catalyzed Enantioselective C(Sp^3)−H Amination: A Combined Computational and Experimental Investigation. *J. Am. Chem. Soc.* **2022**, *144* (25), 11215−11225.
(64) Chatterjee, R.; Jindal, G. Role of Mutations in a Chemoenzymatic Enantiodivergent C(Sp^3)−H Insertion: Exploring the Mechanism and Origin of Stereoselectivity. *Chem. Sci.* **2023**, *14* (33), 8810−8822.
(65) Nakano, Y.; Biegasiewicz, K. F.; Hyster, T. K. Biocatalytic Hydrogen Atom Transfer: An Invigorating Approach to Free-Radical Reactions. *Curr. Opin. Chem. Biol.* **2019**, *49*, 16−24.
(66) Chaturvedi, S. S.; Rifayee, S. B. J. S.; Waheed, S. O.; Wildey, J.; Warner, C.; Schofield, C. J.; Karabencheva-Christova, T. G.; Christov, C. Z. Can Second Coordination Sphere and Long-Range Interactions Modulate Hydrogen Atom Transfer in a Non-Heme Fe(II)-Dependent Histone Demethylase? *JACS Au* **2022**, *2* (9), 2169−2186.
(67) Schwede, T. SWISS-MODEL: An Automated Protein Homology-Modeling Server. *Nucleic Acids Res.* **2003**, *31* (13), 3381−3385.
(68) Gordon, J. C.; Myers, J. B.; Folta, T.; Shoja, V.; Heath, L. S.; Onufriev, A. H++: A Server for Estimating pKas and Adding Missing Hydrogens to Macromolecules. *Nucleic Acids Res.* **2005**, *33*, W368−W371.
(69) Li, P.; Merz, K. M. MCPB.Py: A Python Based Metal Center Parameter Builder. *J. Chem. Inf. Model.* **2016**, *56* (4), 599−604.
(70) Wang, J.; Wang, W.; Kollman, P. A.; Case, D. A. Automatic Atom Type and Bond Type Perception in Molecular Mechanical Calculations. *J. Mol. Graphics Modell.* **2006**, *25* (2), 247−260.
(71) Salomon-Ferrer, R.; Götz, A. W.; Poole, D.; Le Grand, S.; Walker, R. C. Routine Microsecond Molecular Dynamics Simulations with AMBER on GPUs. 2. Explicit Solvent Particle Mesh Ewald. *J. Chem. Theory Comput.* **2013**, *9* (9), 3878−3888.
(72) Jorgensen, W. L.; Chandrasekhar, J.; Madura, J. D.; Impey, R. W.; Klein, M. L. Comparison of Simple Potential Functions for Simulating Liquid Water. *J. Chem. Phys.* **1983**, *79* (2), 926−935.
(73) Borowski, T.; Bassan, A.; Siegbahn, P. E. M. Mechanism of Dioxygen Activation in 2-Oxoglutarate-Dependent Enzymes: A Hybrid DFT Study. *Chem. - Eur. J.* **2004**, *10* (4), 1031−1041.

https://doi.org/10.1021/acs.inorgchem.4c01365
Inorg. Chem. 2024, 63, 10737−10755

(74) Krebs, C.; Fujimori, D. G.; Walsh, C. T.; Bollinger, J. M. Non-Heme Fe(IV)−Oxo Intermediates. *Acc. Chem. Res.* **2007**, *40* (7), 484−492.
(75) Solomon, E. I. Geometric and Electronic Structure Contributions to Function in Bioinorganic Chemistry: Active Sites in Non-Heme Iron Enzymes. *Inorg. Chem.* **2001**, *40* (15), 3656−3669.
(76) Quesne, M. G.; Latifi, R.; Gonzalez-Ovalle, L. E.; Kumar, D.; de Visser, S. P. Quantum Mechanics/Molecular Mechanics Study on the Oxygen Binding and Substrate Hydroxylation Step in AlkB Repair Enzymes. *Chem. - Eur. J.* **2014**, *20* (2), 435−446.
(77) Lee, N. Y.; Mandal, D.; Bae, S. H.; Seo, M. S.; Lee, Y.-M.; Shaik, S.; Cho, K.-B.; Nam, W. Structure and Spin State of Nonheme Fe ^{IV} O Complexes Depending on Temperature: Predictive Insights from DFT Calculations and Experiments. *Chem. Sci.* **2017**, *8* (8), 5460−5467.
(78) Solomon, E. I.; Light, K. M.; Liu, L. V.; Srnec, M.; Wong, S. D. Geometric and Electronic Structure Contributions to Function in Non-Heme Iron Enzymes. *Acc. Chem. Res.* **2013**, *46* (11), 2725−2739.
(79) Maier, J. A.; Martinez, C.; Kasavajhala, K.; Wickstrom, L.; Hauser, K. E.; Simmerling, C. ff14SB: Improving the Accuracy of Protein Side Chain and Backbone Parameters from ff99SB. *J. Chem. Theory Comput.* **2015**, *11* (8), 3696−3713.
(80) Deserno, M.; Holm, C. How to Mesh up Ewald Sums. I. A Theoretical and Numerical Comparison of Various Particle Mesh Routines. *J. Chem. Phys.* **1998**, *109* (18), 7678−7693.
(81) Davidchack, R. L.; Ouldridge, T. E.; Tretyakov, M. V. New Langevin and Gradient Thermostats for Rigid Body Dynamics. *J. Chem. Phys.* **2015**, *142* (14), No. 144114.
(82) Bresme, F. Equilibrium and Nonequilibrium Molecular-Dynamics Simulations of the Central Force Model of Water. *J. Chem. Phys.* **2001**, *115* (16), 7564−7574.
(83) Ryckaert, J.-P.; Ciccotti, G.; Berendsen, H. J. C. Numerical Integration of the Cartesian Equations of Motion of a System with Constraints: Molecular Dynamics of n-Alkanes. *J. Comput. Phys.* **1977**, *23* (3), 327−341.
(84) Torabifard, H.; Cisneros, G. A. Computational Investigation of O_2 Diffusion through an Intra-Molecular Tunnel in AlkB; Influence of Polarization on O_2 Transport. *Chem. Sci.* **2017**, *8* (9), 6230−6238.
(85) Domene, C.; Jorgensen, C.; Schofield, C. J. Mechanism of Molecular Oxygen Diffusion in a Hypoxia-Sensing Prolyl Hydroxylase Using Multiscale Simulation. *J. Am. Chem. Soc.* **2020**, *142* (5), 2253−2263.
(86) Chaturvedi, S. S.; Thomas, M. G.; Rifayee, S. B. J. S.; White, W.; Wildey, J.; Warner, C.; Schofield, C. J.; Hu, J.; Hausinger, R. P.; Karabencheva-Christova, T. G.; Christov, C. Z. Dioxygen Binding Is Controlled by the Protein Environment in Non-heme Fe ^{II} and 2-Oxoglutarate Oxygenases: A Study on Histone Demethylase PHF8 and an Ethylene-Forming Enzyme. *Chem. - Eur. J.* **2023**, *29* (24), No. e202300138.
(87) Martínez, L.; Andrade, R.; Birgin, E. G.; Martínez, J. M. P ACKMOL : A Package for Building Initial Configurations for Molecular Dynamics Simulations. *J. Comput. Chem.* **2009**, *30* (13), 2157−2164.
(88) Humphrey, W.; Dalke, A.; Schulten, K. VMD: Visual Molecular Dynamics. *J. Mol. Graphics* **1996**, *14* (1), 33−38.
(89) Chovancova, E.; Pavelka, A.; Benes, P.; Strnad, O.; Brezovsky, J.; Kozlikova, B.; Gora, A.; Sustr, V.; Klvana, M.; Medek, P.; Biedermannova, L.; Sochor, J.; Damborsky, J. CAVER 3.0: A Tool for the Analysis of Transport Pathways in Dynamic Protein Structures. *PLoS Comput. Biol.* **2012**, *8* (10), No. e1002708.
(90) Metz, S.; Kästner, J.; Sokol, A. A.; Keal, T. W.; Sherwood, P. ChemShell—a Modular Software Package for QM/MM Simulations. *WIREs Comput. Mol. Sci.* **2014**, *4* (2), 101−110.
(91) Ahlrichs, R.; Bär, M.; Häser, M.; Horn, H.; Kölmel, C. Electronic Structure Calculations on Workstation Computers: The Program System Turbomole. *Chem. Phys. Lett.* **1989**, *162* (3), 165−169.
(92) Smith, W.; Yong, C. W.; Rodger, P. M. DL_POLY: Application to Molecular Simulation. *Mol. Simul.* **2002**, *28* (5), 385−471.
(93) Bakowies, D.; Thiel, W. Hybrid Models for Combined Quantum Mechanical and Molecular Mechanical Approaches. *J. Phys. Chem. A* **1996**, *100* (25), 10580−10594.
(94) Becke, A. D. Density-Functional Thermochemistry. III. The Role of Exact Exchange. *J. Chem. Phys.* **1993**, *98* (7), 5648−5652.
(95) Que, L. The Road to Non-Heme Oxoferryls and Beyond. *Acc. Chem. Res.* **2007**, *40* (7), 493−500.
(96) Hong, S.; Sutherlin, K. D.; Park, J.; Kwon, E.; Siegler, M. A.; Solomon, E. I.; Nam, W. Crystallographic and Spectroscopic Characterization and Reactivities of a Mononuclear Non-Haem Iron(III)-Superoxo Complex. *Nat. Commun.* **2014**, *5* (1), No. 5440.
(97) Song, X.; Lu, J.; Lai, W. Mechanistic Insights into Dioxygen Activation, Oxygen Atom Exchange and Substrate Epoxidation by AsqJ Dioxygenase from Quantum Mechanical/Molecular Mechanical Calculations. *Phys. Chem. Chem. Phys.* **2017**, *19* (30), 20188−20197.
(98) Ye, S.; Riplinger, C.; Hansen, A.; Krebs, C.; Bollinger, J. M.; Neese, F. Electronic Structure Analysis of the Oxygen-Activation Mechanism by Fe ^{II} - and α-Ketoglutarate (αKG)-Dependent Dioxygenases. *Chem. - Eur. J.* **2012**, *18* (21), 6555−6567.
(99) Wójcik, A.; Radoń, M.; Borowski, T. Mechanism of O $_2$ Activation by α-Ketoglutarate Dependent Oxygenases Revisited. A Quantum Chemical Study. *J. Phys. Chem. A* **2016**, *120* (8), 1261−1274.
(100) Bassan, A.; Borowski, T.; Siegbahn, P. E. M. Quantum Chemical Studies of Dioxygen Activation by Mononuclear Non-Heme Iron Enzymes with the 2-His-1-Carboxylate Facial Triad. *Dalton Trans.* **2004**, No. 20, 3153−3162.
(101) Saura, P.; Röpke, M.; Gamiz-Hernandez, A. P.; Kaila, V. R. I. Quantum Chemical and QM/MM Models in Biochemistry. In *Methods in Molecular Biology*; Bonomi, M.; Camilloni, C., Eds.; Springer New York: New York, NY, 2019; Vol. *2022*, pp 75−104.
(102) Eichkorn, K.; Weigend, F.; Treutler, O.; Ahlrichs, R. Auxiliary Basis Sets for Main Row Atoms and Transition Metals and Their Use to Approximate Coulomb Potentials. *Theor. Chem. Acc.* **1997**, *97* (1−4), 119−124.
(103) Kästner, J.; Carr, J. M.; Keal, T. W.; Thiel, W.; Wander, A.; Sherwood, P. DL-FIND: An Open-Source Geometry Optimizer for Atomistic Simulations. *J. Phys. Chem. A* **2009**, *113* (43), 11856−11865.
(104) Ramanan, R.; Dubey, K. D.; Wang, B.; Mandal, D.; Shaik, S. Emergence of Function in P450-Proteins: A Combined Quantum Mechanical/Molecular Mechanical and Molecular Dynamics Study of the Reactive Species in the H_2O_2-Dependent Cytochrome P450 $_{SP\alpha}$ and Its Regio- and Enantioselective Hydroxylation of Fatty Acids. *J. Am. Chem. Soc.* **2016**, *138* (21), 6786−6797.
(105) Schäfer, A.; Horn, H.; Ahlrichs, R. Fully Optimized Contracted Gaussian Basis Sets for Atoms Li to Kr. *J. Chem. Phys.* **1992**, *97* (4), 2571−2577.
(106) Ramanan, R.; Waheed, S. O.; Schofield, C. J.; Christov, C. Z. What Is the Catalytic Mechanism of Enzymatic Histone N-Methyl Arginine Demethylation and Can It Be Influenced by an External Electric Field? *Chem. - Eur. J.* **2021**, *27* (46), 11827−11836.
(107) Waheed, S. O.; Chaturvedi, S. S.; Karabencheva-Christova, T. G.; Christov, C. Z. Catalytic Mechanism of Human Ten-Eleven Translocation-2 (TET2) Enzyme: Effects of Conformational Changes, Electric Field, and Mutations. *ACS Catal.* **2021**, *11* (7), 3877−3890.
(108) Varghese, A.; Waheed, S. O.; Chaturvedi, S. S.; DiCastri, I.; LaRouche, C.; Kaski, B.; Lehnert, N.; Li, D.; Christov, C. Z.; Karabencheva-Christova, T. G. Revealing the Catalytic Strategy of FTO. *Chem. Catal.* **2023**, *3* (9), No. 100732.
(109) Roy, S.; Kästner, J. Catalytic Mechanism of Salicylate Dioxygenase: QM/MM Simulations Reveal the Origin of Unexpected Regioselectivity of the Ring Cleavage. *Chem. - Eur. J.* **2017**, *23* (37), 8949−8962.
(110) Park, K.; Li, N.; Kwak, Y.; Srnec, M.; Bell, C. B.; Liu, L. V.; Wong, S. D.; Yoda, Y.; Kitao, S.; Seto, M.; Hu, M.; Zhao, J.; Krebs, C.;

Bollinger, J. M.; Solomon, E. I. Peroxide Activation for Electrophilic Reactivity by the Binuclear Non-Heme Iron Enzyme AurF. *J. Am. Chem. Soc.* **2017**, *139* (20), 7062−7070.
(111) Srnec, M.; Solomon, E. I. Frontier Molecular Orbital Contributions to Chlorination versus Hydroxylation Selectivity in the Non-Heme Iron Halogenase SyrB2. *J. Am. Chem. Soc.* **2017**, *139* (6), 2396−2407.
(112) Cortopassi, W. A.; Simion, R.; Honsby, C. E.; França, T. C. C.; Paton, R. S. Dioxygen Binding in the Active Site of Histone Demethylase JMJD2A and the Role of the Protein Environment. *Chem. - Eur. J.* **2015**, *21* (52), 18983−18992.
(113) Zhang, X.; Wang, Z.; Gao, J.; Liu, W. Chlorination *versus* Hydroxylation Selectivity Mediated by the Non-Heme Iron Halogenase WelO5. *Phys. Chem. Chem. Phys.* **2020**, *22* (16), 8699−8712.
(114) Chen, H.; Cho, K.-B.; Lai, W.; Nam, W.; Shaik, S. Dioxygen Activation by a Non-Heme Iron(II) Complex: Theoretical Study toward Understanding Ferric−Superoxo Complexes. *J. Chem. Theory Comput.* **2012**, *8* (3), 915−926.
(115) Meisburger, S. P.; Thomas, W. C.; Watkins, M. B.; Ando, N. X-Ray Scattering Studies of Protein Structural Dynamics. *Chem. Rev.* **2017**, *117* (12), 7615−7672.
(116) Adcock, S. A.; McCammon, J. A. Molecular Dynamics: Survey of Methods for Simulating the Activity of Proteins. *Chem. Rev.* **2006**, *106* (5), 1589−1615.
(117) Davis, A. M.; Teague, S. J.; Kleywegt, G. J. Application and Limitations of X-ray Crystallographic Data in Structure-Based Ligand and Drug Design. *Angew. Chem., Int. Ed.* **2003**, *42* (24), 2718−2736.
(118) Karplus, M.; Kuriyan, J. Molecular Dynamics and Protein Function. *Proc. Natl. Acad. Sci. U.S.A.* **2005**, *102* (19), 6679−6685.
(119) Bui, S.; Gil-Guerrero, S.; van der Linden, P.; Carpentier, P.; Ceccarelli, M.; Jambrina, P. G.; Steiner, R. A. Evolutionary Adaptation from Hydrolytic to Oxygenolytic Catalysis at the α/β-Hydrolase Fold. *Chem. Sci.* **2023**, *14* (38), 10547−10560.
(120) Tsai, C.-L.; Shi, Y.; Tainer, J. A. How Substrate Specificity Is Imposed on a Histone Demethylase—Lessons from KDM2A. *Genes Dev.* **2014**, *28* (16), 1735−1738.
(121) Georgiev, V.; Borowski, T.; Blomberg, M. R. A.; Siegbahn, P. E. M. A Comparison of the Reaction Mechanisms of Iron- and Manganese-Containing 2,3-HPCD: An Important Spin Transition for Manganese. *JBIC, J. Biol. Inorg. Chem.* **2008**, *13* (6), 929−940.
(122) Graham, S. E.; Syeda, F.; Cisneros, G. A. Computational Prediction of Residues Involved in Fidelity Checking for DNA Synthesis in DNA Polymerase I. *Biochemistry* **2012**, *51* (12), 2569−2578.
(123) Torabifard, H.; Cisneros, G. A. Insight into Wild-Type and T1372E TET2-Mediated 5hmC Oxidation Using *Ab Initio* QM/MM Calculations. *Chem. Sci.* **2018**, *9* (44), 8433−8445.
(124) Cisneros, G. A.; Perera, L.; Schaaper, R. M.; Pedersen, L. C.; London, R. E.; Pedersen, L. G.; Darden, T. A. Reaction Mechanism of the ε Subunit of *E. coli* DNA Polymerase III: Insights into Active Site Metal Coordination and Catalytically Significant Residues. *J. Am. Chem. Soc.* **2009**, *131* (4), 1550−1556.
(125) Srnec, M.; Iyer, S. R.; Dassama, L. M. K.; Park, K.; Wong, S. D.; Sutherlin, K. D.; Yoda, Y.; Kobayashi, Y.; Kurokuzu, M.; Saito, M.; Seto, M.; Krebs, C.; Bollinger, J. M.; Solomon, E. I. Nuclear Resonance Vibrational Spectroscopic Definition of the Facial Triad Fe^{IV}═O Intermediate in Taurine Dioxygenase: Evaluation of Structural Contributions to Hydrogen Atom Abstraction. *J. Am. Chem. Soc.* **2020**, *142* (44), 18886−18896.
(126) Roy, L. Theoretical Identification of the Factors Governing the Reactivity of C−H Bond Activation by Non-Heme Iron(IV)-Oxo Complexes. *ChemPlusChem* **2019**, *84* (7), 893−906.
(127) Sun, X.; Geng, C.; Huo, R.; Ryde, U.; Bu, Y.; Li, J. Large Equatorial Ligand Effects on C−H Bond Activation by Nonheme Iron(IV)-Oxo Complexes. *J. Phys. Chem. B* **2014**, *118* (6), 1493−1500.
(128) Shaik, S.; Kumar, D.; De Visser, S. P.; Altun, A.; Thiel, W. Theoretical Perspective on the Structure and Mechanism of Cytochrome P450 Enzymes. *Chem. Rev.* **2005**, *105* (6), 2279−2328.
(129) Shaik, S.; Chen, H.; Janardanan, D. Exchange-Enhanced Reactivity in Bond Activation by Metal−Oxo Enzymes and Synthetic Reagents. *Nat. Chem.* **2011**, *3* (1), 19−27.
(130) Ye, S.; Neese, F. Quantum Chemical Studies of C−H Activation Reactions by High-Valent Nonheme Iron Centers. *Curr. Opin. Chem. Biol.* **2009**, *13* (1), 89−98.
(131) Ghafoor, S.; Mansha, A.; De Visser, S. P. Selective Hydrogen Atom Abstraction from Dihydroflavonol by a Nonheme Iron Center Is the Key Step in the Enzymatic Flavonol Synthesis and Avoids Byproducts. *J. Am. Chem. Soc.* **2019**, *141* (51), 20278−20292.
(132) Solomon, E. I.; Goudarzi, S.; Sutherlin, K. D. O_2 Activation by Non-Heme Iron Enzymes. *Biochemistry* **2016**, *55* (46), 6363−6374.
(133) Solomon, E. I.; Wong, S. D.; Liu, L. V.; Decker, A.; Chow, M. S. Peroxo and Oxo Intermediates in Mononuclear Nonheme Iron Enzymes and Related Active Sites. *Curr. Opin. Chem. Biol.* **2009**, *13* (1), 99−113.
(134) Wong, S. D.; Srnec, M.; Matthews, M. L.; Liu, L. V.; Kwak, Y.; Park, K.; Bell, C. B., III; Alp, E. E.; Zhao, J.; Yoda, Y.; Kitao, S.; Seto, M.; Krebs, C.; Bollinger, J. M.; Solomon, E. I. Elucidation of the Fe(Iv)═O Intermediate in the Catalytic Cycle of the Halogenase SyrB2. *Nature* **2013**, *499* (7458), 320−323.
(135) Mandal, D.; Mallick, D.; Shaik, S. Kinetic Isotope Effect Determination Probes the Spin of the Transition State, Its Stereochemistry, and Its Ligand Sphere in Hydrogen Abstraction Reactions of Oxoiron(IV) Complexes. *Acc. Chem. Res.* **2018**, *51* (1), 107−117.
(136) De Visser, S. P. Second-Coordination Sphere Effects on Selectivity and Specificity of Heme and Nonheme Iron Enzymes. *Chem. - Eur. J.* **2020**, *26* (24), 5308−5327.
(137) Ali, H. S.; Henchman, R. H.; Warwicker, J.; De Visser, S. P. How Do Electrostatic Perturbations of the Protein Affect the Bifurcation Pathways of Substrate Hydroxylation versus Desaturation in the Nonheme Iron-Dependent Viomycin Biosynthesis Enzyme? *J. Phys. Chem. A* **2021**, *125* (8), 1720−1737.
(138) Sahu, S.; Widger, L. R.; Quesne, M. G.; De Visser, S. P.; Matsumura, H.; Moënne-Loccoz, P.; Siegler, M. A.; Goldberg, D. P. Secondary Coordination Sphere Influence on the Reactivity of Nonheme Iron(II) Complexes: An Experimental and DFT Approach. *J. Am. Chem. Soc.* **2013**, *135* (29), 10590−10593.
(139) Yeh, C. G.; Mokkawes, T.; Bradley, J. M.; Le Brun, N. E.; De Visser, S. P. Second Coordination Sphere Effects on the Mechanistic Pathways for Dioxygen Activation by a Ferritin: Involvement of a Tyr Radical and the Identification of a Cation Binding Site. *ChemBioChem* **2022**, *23* (13), No. e202200257.
(140) Kastner, D. W.; Nandy, A.; Mehmood, R.; Kulik, H. J. Mechanistic Insights into Substrate Positioning That Distinguish Non-Heme Fe(II)/α-Ketoglutarate-Dependent Halogenases and Hydroxylases. *ACS Catal.* **2023**, *13* (4), 2489−2501.
(141) Wojdyla, Z.; Borowski, T. Enzyme Multifunctionality by Control of Substrate Positioning Within the Catalytic Cycle—A QM/MM Study of Clavaminic Acid Synthase. *Chem. - Eur. J.* **2021**, *27* (6), 2196−2211.
(142) Álvarez-Barcia, S.; Kästner, J. Atom Tunneling in the Hydroxylation Process of Taurine/α-Ketoglutarate Dioxygenase Identified by Quantum Mechanics/Molecular Mechanics Simulations. *J. Phys. Chem. B* **2017**, *121* (21), 5347−5354.
(143) Godfrey, E.; Porro, C. S.; de Visser, S. P. Comparative Quantum Mechanics/Molecular Mechanics (QM/MM) and Density Functional Theory Calculations on the Oxo−Iron Species of Taurine/α-Ketoglutarate Dioxygenase. *J. Phys. Chem. A* **2008**, *112* (11), 2464−2468.

https://doi.org/10.1021/acs.inorgchem.4c01365
Inorg. Chem. 2024, 63, 10737−10755